

# Efficient quantum dot $\mathbf{k} \cdot \mathbf{p}$ in wurtzite systems including spatially varying elastic and dielectric constants and smooth alloy profile

Luc Robichaud<sup>1</sup> and Jacob J. Krich<sup>1,2</sup>

<sup>1</sup>*Department of Physics, University of Ottawa, Ottawa, Canada K1N 6N5 and*

<sup>2</sup>*School of Electrical Engineering and Computer Science,  
University of Ottawa, Ottawa, Canada K1N 6N5*

(Dated: 16 December 2020)

We present Fourier-space based methods to calculate the electronic structure of wurtzite quantum dot systems with continuous alloy profiles. We incorporate spatially varying elastic and dielectric constants in strain and piezoelectric potential calculations. A method to incorporate smooth alloy profiles in all aspects of the calculations is presented. We demonstrate our methodology for the case of a 1D InGaN quantum dot array and show the importance of including these spatially varying parameters in the modeling of devices. We demonstrate that convergence of the lowest bound state energies is to good approximation determined by the largest wave vector used in constructing the states. We also present a novel approach of coupling strain into the  $\mathbf{k} \cdot \mathbf{p}$  Hamiltonian, greatly reducing the computational cost of generating the Hamiltonian.

## I. INTRODUCTION

Given their large range of bandgaps, from 0.78 eV to 3.51 eV, InGaN materials have attracted attention from various applications such as LEDs, single-photon emitters, water splitting and solar cells [1–5]. For any application, device performance depends on having an electronic structure well tuned to its target application. Given that the electronic structure of quantum dots can be drastically changed by varying their size and composition, they can be quite attractive for applications. The main problem in modeling complex structures such as quantum dots is including all the necessary effects for the model to be accurate while also keeping computational cost down.

Tight binding and  $\mathbf{k} \cdot \mathbf{p}$  theory are standard approaches for calculating single-particle electronic structures for bulk materials and nanostructures [6]. The  $\mathbf{k} \cdot \mathbf{p}$  method gives a good balance between accuracy and computational requirements, especially when considering large dots that contain large number of atoms where the tight binding method becomes costly.  $\mathbf{k} \cdot \mathbf{p}$  theory has been developed in both real space and Fourier space [7, 8]. Following the Fourier-space method, symmetry adapted basis approaches have been developed to reduce the required size of the Hamiltonian, which block diagonalize the Hamiltonian, reducing the computational cost of calculating the system's eigenstates [9–11].

InGaN materials are strongly piezoelectric, having both spontaneous and strain-induced contributions to the piezoelectric polarization. Strain calculations have been performed using valence force field and Green's function based methods [8, 12]. The latter method has the advantage that it respects the symmetry of the crystal lattice. From the strain, the piezoelectric potential can be calculated from Maxwell's equations [8]. References [8, 10, 13] use the Green's function method for calculating strain and calculated the piezoelectric potential from Maxwell's equations. These works assume uniform elastic and dielectric constants, which was justified for their respective InAs/GaAs and GaN/AlN systems. However, in the case of InGaN, these constants vary more significantly between dot and host. Additionally, InGaN devices frequently do not have sharp interfaces between dot and barrier, with indium diffusing over several nanometers. This smooth alloy profile gives a spatial profile to every material parameter of the system, effectively changing the confining potential seen by the electrons.

In this paper, we show the importance of including spatially varying elastic and dielectric constants in strain and piezoelectric potential calculations in the case InGaN systems. For strain calculations, we implement a formalism previously presented for including spatially varying elastic constants [8]. We present a new Fourier-space formalism for the calculation of piezoelectric potentials with spatially varying dielectric constants. We also present an approach to include smooth indium profiles in the strain, piezoelectric potential and electronic structure calculations, modeling the smooth alloy profiles found in experimental devices. Considering smooth indium profiles both increase the accuracy of the simulations and decrease their computational cost by decreasing the number of plane waves required for convergence.

Strain plays an important role in the electronic structure properties of quantum dots. In quantum dot  $\mathbf{k} \cdot \mathbf{p}$ , a single real space unit cell is typically used when working in a Fourier-space approach. However, strain decays more slowly than bound state wavefunctions. When studying isolated dots, the difference in decay lengths makes it computationally expensive to fully capture both the strain and electronic structure using a single unit cell. Reference [11] presents an approach that implements two different unit cells; one for the electronic structure and one for strain. This method allows for the modeling of the electronic structure and strain, but introduces some complexity in calculating the

Hamiltonian, which requires the calculation of multiple composed convolutions on different Fourier-space meshes. These convolutions can be computationally costly depending on the sizes of meshes needed for convergence. By fixing the strain unit cell to be commensurate with the electronic unit cell, we present an approach that reduces the number of needed convolutions, significantly reducing the computational cost.

We demonstrate our methodology by calculating the electronic structure for a 1D array of InGaN quantum dots, modeling devices grown as LEDs and for water splitting [1, 3]. In this example, we show the importance of the inclusion of spatially varying elastic and dielectric constants and smooth indium profiles for accurate electronic structures. We also show that the most important criterion for convergence of the lowest quantum dot electron and hole energies is the maximum wave vector included in the Fourier-space sampling, which can be increased with low computational cost by using a small unit cell.

Section II contains strain and piezoelectric potential calculations using spatially varying elastic and dielectric parameters. Section III presents the  $\mathbf{k} \cdot \mathbf{p}$  model used for electronic structure calculations and our novel approach to efficiently include strain through choices of unit cells. Section IV introduces a method to use smooth indium profiles in all aspects of our calculations. Section V demonstrates our entire methodology for the case of a 1D quantum dot array, such as quantum dots grown inside of nanowires [1].

## II. SPATIALLY VARYING ELASTIC AND PIEZOELECTRIC CONSTANTS CORRECTIONS

We begin by considering quantum dot heterostructures with abrupt changes in alloy fraction. Alloying the host material changes the local lattice constants, leading to a lattice mismatch at the host and dot material boundary. This lattice mismatch is a source of strain throughout the QD system, affecting the electronic states of the system. For example, InN has a larger lattice constant than GaN, so alloying GaN with indium to form quantum dots induces change in the lattice constant. Additionally, strain can generate strong piezoelectric potentials in materials such as III-nitrides. The piezoelectric potential in III-nitrides is particularly important along the *c*-axis and can be strong enough to spatially separate electron and hole states through the quantum-confined Stark effect [14].

In prior work, elastic and dielectric constants are largely assumed to be spatially uniform in Fourier-based calculations of strain and the piezoelectric potential. In fact, these material properties are different in the dot and host materials, which can cause significant errors when determining electronic structures. Here, we calculate the strain and piezoelectric potential of a quantum dot superlattice with elastic and dielectric constants that vary with alloy fraction, while focusing on the changes brought on by spatially changing parameters. In the case of the spatially varying elastic constants, we use a method outlined in Ref. [8]. We present a version with typos in Eqs. A3, A7 and A8 of Ref. [8] corrected in Section II B. For the piezoelectric potential, we use a procedure similar to Ref. [8], but we construct a theory to include spatially varying dielectric constants. The strain field and piezoelectric potential are coupled into a  $\mathbf{k} \cdot \mathbf{p}$  model, presented in Section III, for electronic structure calculations.

### A. Quantum dot system

We consider a superlattice of cylindrical wurtzite quantum dots embedded in a bulk host material, as shown in Fig. 1. InGaN quantum dots such as those described in Ref. [1] have a lens-like shape and do not have a sharply defined boundary. We approximate these quantum dots as being cylindrical. This choice of dot geometry simplifies calculations, as described in Sec. II B, and preserves the  $C_{6v}$  symmetry of the material, which we take advantage of in Section III for electronic structure calculations. Hexagonal periodic boundary conditions are used to also preserve the material's  $C_{6v}$  symmetry. For single-dot calculations, the superlattice unit cell must be large enough that the choice of cell size does not affect results. For actual quantum dot arrays, we consider only hexagonal superlattices in the plane.

In this periodic system, the real space quantum dot superlattice is defined by the set of lattice vectors  $\mathbf{L}_i$ , as shown in Fig. 1. We denote the real space unit cell by  $\Omega_e$ , its volume  $V_e$ , and the reciprocal-space unit cell by  $\Omega_e^{-1}$ . The index “e” indicates that these quantities relate to the electronic cell, as opposed to the strain unit cell, which is introduced in Section III C. Imposing periodic conditions in real space implies a discrete reciprocal space with wave vectors

$$\mathbf{q} = i_1 \mathbf{b}_1 + i_2 \mathbf{b}_2 + i_3 \mathbf{b}_3 \quad i_1, i_2, i_3 \in \mathbb{Z} \quad (1)$$

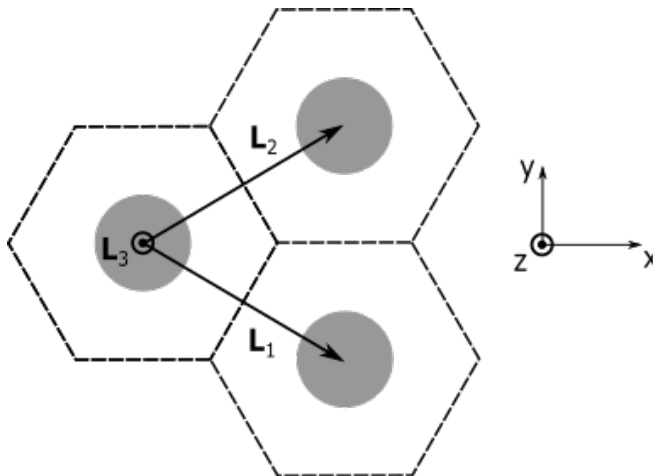


FIG. 1. Quantum dot superlattice and its basis vectors. White regions are the host material and grey regions are the quantum dots. Dashed lines show the unit cell boundaries of the quantum dot superlattice. Due to the symmetry, we have  $L_{12} \equiv |\mathbf{L}_1| = |\mathbf{L}_2|$ .

with the reciprocal basis vectors

$$\begin{aligned}
 \mathbf{b}_1 &= \frac{2\pi}{L_1} \left[ 1, -\frac{1}{\sqrt{3}}, 0 \right] \\
 \mathbf{b}_2 &= \frac{2\pi}{L_2} \left[ 1, \frac{1}{\sqrt{3}}, 0 \right] \\
 \mathbf{b}_3 &= \frac{2\pi}{L_3} [0, 0, 1]
 \end{aligned} \tag{2}$$

Due to the symmetry of the system, we have  $L_1 = L_2$ , which we define as  $L_{12}$ . In our reciprocal-space calculations, we sample on sets of the wave vectors  $\mathbf{q} \in \Omega_{\mathbf{e}}^{-1}$ . We define  $m_{12}$  and  $m_3$  such that  $i_1, i_2 = \{-m_{12}, \dots, 0, \dots, m_{12}\}$  and  $i_3 = \{-m_3, \dots, 0, \dots, m_3\}$ . This sampling produces a hexagonal mesh of size  $N = N_1 N_2 N_3$  where  $N_i = 2m_i + 1$ . To obtain a  $C_6$  symmetric mesh, we remove points such that  $|q_x| > m_{12} \frac{2\pi}{L_1}$ , leaving a mesh whose size we denote by  $N_{\mathbf{e}}$ .

By choosing the unit cell dimensions  $L_i$  large enough, it is possible to remove electronic coupling between neighboring dots. This flexibility allows us to model 3D, 2D and 1D arrays of coupled dots. The isolated dot case can also be obtained by choosing both  $L_{12}$  and  $L_3$  sufficiently large. Section II B presents a method that also uncouples dots in terms of strain, which is based on calculating strain and the electronic structure using different unit cells.

We illustrate the methods presented in this manuscript by modeling a quantum dot system inspired by Ref. [1]. That system consists of InGaN dots grown in GaN nanowires. We approximate this system as a 1D quantum dot array, by choosing  $L_3$  to match the measured dot-dot spacing and  $L_{12}$  large enough to avoid dot-dot coupling. We fix the dot indium alloy fraction, radius and height based on the experimental device. System parameters are listed in Table I and material parameters are in Appendix A.

## B. Strain

In this section, we present how we calculate strain with elastic constants that depend on alloy fraction for 3D, 2D and 1D quantum dot superlattices and isolated dots. Our method follows from Refs. [8, 11].

Materials such as InGaN have elastic constants that vary based on the alloy fraction. Therefore, the spatial variation of the elastic constants throughout the superlattice unit cell must be included for accurate calculations of strain. We present a method, originally derived in Ref. [8], to include spatially varying elastic constants in strain calculations. We calculate the strain produced by a single isolated dot and construct the quantum dot superlattice strain by linear superposition.

The calculated strain is to be coupled into the electronic structure calculations. However, strain decays considerably slower than bound electronic wavefunctions. In the case of isolated dots, the unit cell must be large enough to accommodate the strain decay. Choosing a unit cell large enough to capture the strain decay reduces the maximum wave vector attainable when using a fixed number of plane waves. As we demonstrate in Section V, accurately

TABLE I. Quantum dot superlattice system parameters used for calculations unless specified otherwise.

Parameter	Value
$X_0$	0.45
$h$	40 $\text{\AA}$
$R$	200 $\text{\AA}$
$L_{12}$	500 $\text{\AA}$
$L_3$	70 $\text{\AA}$
$m_{12}$	10
$m_3$	4
$n_{12}$	6
$n_3$	1
$\delta$	[1.5, 1.5, 2.5] $\text{\AA}$

describing the electronic states requires using sufficiently large wave vectors, and thus a large unit cell requires a large number of plane waves. Following Ref. [11], we consider that the electronic model and strain model each have their own real space unit cells. This additional degree of freedom allows accurate and computationally efficient determination of both electronic structure of rapidly decaying confined quantum dot states and longer-range strain effects in isolated dots. In the case of a quantum dot superlattice, different real-space electronic and strain unit cells are not required.

### 1. Isolated quantum dot strain

In prior work, lattice-mismatch-driven strain has been calculated for a single dot using a continuum theory with a Green's function approach while assuming spatially uniform elastic constants [8, 13, 15]. Here, we present the method outlined in Appendix A of [8] to include spatially varying elastic constants. In this section, we show how the spatially varying elastic constants modify strain and how this modified strain changes the piezoelectric potential in Section II C. We show that the elastic constant correction is necessary to obtain accurate strain and piezoelectric potentials.

Consider a single InGaN QD in bulk GaN with spatially varying elastic constants  $\lambda_{ijmn}(\mathbf{r})$  that depend on the local alloy fraction,

$$\lambda_{ijmn}(\mathbf{r}) = \lambda_{ijmn}^d + \lambda_{ijmn}^h [1 - \chi_d(\mathbf{r})], \quad (3)$$

where  $\lambda_{ijmn}^h$  and  $\lambda_{ijmn}^d$  are the host and dot's elastic constants, respectively. Assuming spatially varying elastic constants, the Green's tensor  $\tilde{G}_{in}$  for the displacement field in an infinite anisotropic elastic medium must satisfy

$$\frac{\partial}{\partial x_k} \lambda_{iklm}(\mathbf{r}) \frac{\partial}{\partial x_m} G(\mathbf{r}, \mathbf{r}') = -\delta(\mathbf{r} - \mathbf{r}') \delta_{in} \quad (4)$$

Taking the Fourier transform of Eq. 4, we obtain

$$\begin{aligned} & \lambda_{iklm}^h q_k q_m \tilde{G}_{ln}(\mathbf{q}, \mathbf{r}') \\ & + \Delta \lambda_{iklm} \sum_{\mathbf{q}'} \tilde{\chi}_d(\mathbf{q} - \mathbf{q}') q_k q'_m \tilde{G}_{ln}(\mathbf{q}', \mathbf{r}') \\ & = \frac{1}{(2\pi)^3} e^{i\mathbf{q}\cdot\mathbf{r}'} \delta_{in}. \end{aligned}$$

The system strain is given by the superposition  $\tilde{\epsilon}_{lm}(\mathbf{q}) = e_{lm}^T \tilde{\chi}_d(\mathbf{q}) + \tilde{\epsilon}_{lm}^c(\mathbf{q})$  where  $e_{lm}^T$  is the stress-free strain due to the initial lattice mismatch and  $\tilde{\epsilon}_{lm}^c$  is the interface-driven strain [8, 13]. Reference [8] showed that the Green's tensor can be related to the strain  $\tilde{\epsilon}_{lm}^c(\mathbf{q})$  to obtain

$$\begin{aligned} & \lambda_{iklm}^h q_k \tilde{\epsilon}_{lm}^c(\mathbf{q}) \\ & + \Delta \lambda_{iklm} q_k \sum_{\mathbf{q}'} \tilde{\chi}_d(\mathbf{q} - \mathbf{q}') \tilde{\epsilon}_{lm}^c(\mathbf{q}') \\ & = -\lambda_{ikpr}^d \tilde{\epsilon}_{pr}^T q_k \tilde{\chi}^d(\mathbf{q}), \end{aligned} \quad (5)$$

with typos fixed, where  $\chi_d$  is the characteristic function of the dot, which is unity inside the dot and zero outside (see Appendix B for its Fourier transform in our case of cylindrical dots), and  $e_{pr}^T$  is

$$e_{pr}^T = \varepsilon_a \delta_{pr} + \varepsilon_{ca} \delta_{p3} \delta_{r3}$$

with  $\varepsilon_a = (a^h - a^d)/a^d$ ,  $\varepsilon_c = (c^h - c^d)/c^d$  and  $\varepsilon_{ca} = \varepsilon_c - \varepsilon_a$ . Here,  $a^h$ ,  $c^h$  are the lattice constants of the host material and,  $a^d$  and  $c^d$  are of dot material. More specifically,  $a$  is the xy-plane lattice constant and  $c$  is the lattice constant along the z-axis. A solution for  $\tilde{\varepsilon}_{lm}^c(\mathbf{q})$  can be found by expanding  $\tilde{\varepsilon}_{lm}^c(\mathbf{q})$  in a power series,

$$\tilde{\varepsilon}_{lm}^c(\mathbf{q}) = \tilde{\varepsilon}_{lm}^{(0)}(\mathbf{q}) + \tilde{\varepsilon}_{lm}^{(1)}(\mathbf{q}) + \tilde{\varepsilon}_{lm}^{(2)}(\mathbf{q}) + \dots, \quad (6)$$

where  $\tilde{\varepsilon}_{lm}^{(N)}(\mathbf{q}) \propto (\frac{\Delta\lambda}{\lambda})^N$ ,  $\Delta\lambda_{ijmn} = \lambda_{ijmn}^h - \lambda_{ijmn}^d$  and the condition  $\frac{\Delta\lambda}{\lambda} \ll 1$  ensures convergence of the series. The leading term  $\tilde{\varepsilon}_{lm}^{(0)}$  corresponds to uniform elastic constants of the dot with each subsequent term being a correction to include spatial variations due to the alloy profile. Using the Einstein summation convention, each term has the form

$$\tilde{\varepsilon}_{lm}^{(N)}(\mathbf{q}) = \frac{(2\pi)^3}{2} \left[ F_p^{(N)}(\mathbf{q}) q_l \tilde{G}_{mp}^h(\mathbf{q}) + F_p^{(N)}(\mathbf{q}) q_m \tilde{G}_{lp}^h(\mathbf{q}) \right] \quad (7)$$

where

$$F_i^{(0)}(\mathbf{q}) = -\lambda_{ikpr}^d \tilde{\varepsilon}_{pr}^T q_k \tilde{\chi}_d(\mathbf{q}) \quad (8)$$

$$F_i^{(N)}(\mathbf{q}) = -\Delta\lambda_{iklm} q_k \frac{(2\pi)^3}{V} \sum_{\mathbf{q}'} \tilde{\chi}_d(\mathbf{q} - \mathbf{q}') \tilde{\varepsilon}_{lm}^{(N-1)}(\mathbf{q}') \quad (9)$$

where Eqs. 7 and 9 are corrected from Ref. [8]. Here,  $\tilde{G}_{in}^h$  is the Green's tensor for the host material and is fully written out in Appendix D.

It has been shown, when assuming uniform elastic constants, that using the parameters for the host material gives more accurate results. We compare the strain corrected at various orders according to Eq. 6 to the usually considered case of uniform elastic constants of the host material. Figure 2 shows the convergence of the strain corrections for the 1D quantum dot array system described in Section II A. We quantify convergence with the following metric for the norm of the strain:

$$|\tilde{\varepsilon}| = \sqrt{\sum_{m \geq l} \frac{V}{(2\pi)^3} \int d\mathbf{q}^3 |\tilde{\varepsilon}_{lm}(\mathbf{q})|^2} \quad (10)$$

where  $m \geq l$  indicates the sum of the unique elements of the strain tensor ( $\tilde{\varepsilon}_{11}$ ,  $\tilde{\varepsilon}_{22}$ ,  $\tilde{\varepsilon}_{33}$ ,  $\tilde{\varepsilon}_{23}$ ,  $\tilde{\varepsilon}_{13}$ ,  $\tilde{\varepsilon}_{12}$ ). The green line in Fig. 2 compares the norm of the corrected strain  $\tilde{\varepsilon}$ , calculated from Eq. 7, to the norm of the strain  $\tilde{\varepsilon}^{\text{GaN}}$ , which is calculated assuming spatially uniform elastic constants of GaN. Blue line shows the self-convergence of the power series in Eq. 6. From these results, we conclude that a 2nd order correction is sufficient to have strain converged within 1% in self-convergence and that this converged strain differs from the uniform case by about 6%, indicating that the elastic constant corrections are important for accurate strain fields in InGaN systems. In Sec. II C, we show that the calculated piezoelectric potential remains essentially unchanged from 3rd order corrections and up. Given that including these corrections are not computationally costly, we have included 3rd order corrections in all of our calculations unless stated otherwise. Figure 3 shows the hydrostatic strain along a cut through the axis of the dot, showing relaxation of strain inside the dot with each additional correction.

## 2. Quantum dot superlattice strain

Because the strain is linear in stress, the strain produced by the QD superlattice can be obtained from linear superposition of the single-dot strain. However, we want the ability to study dots that are completely uncoupled, both electronically and from strains of the periodic array. Reference [11] proposed a method to allow simultaneous treatment of large unit cell for the strain problem and small unit cell for the electronic problem, which together allow isolated dots to be considered in a computationally tractable manner. In this case of two independent cells,

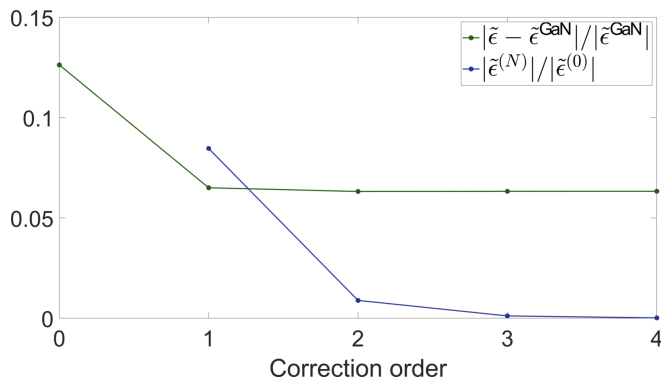


FIG. 2. Convergence of the strain with spatially varying elastic constants. Green line is the relative difference between the corrected strain and the case with uniform  $\lambda$  of GaN for a 1D quantum dot array as described in Table I. The zeroth term is the case of uniform elastic constants of InGaN with alloy fraction of the dot. Converged strain rests at a 6% relative difference from the case of uniform elastic constants of GaN, indicating that the corrections are necessary for accurate strain fields. Blue line is self-convergence of the power series in Eq. 6 in respect to the zeroth term. Correction magnitudes are found to be less than 1% starting from 2nd order. We conclude that corrections up to and including order 3 are sufficient for the calculation of accurate strain fields.

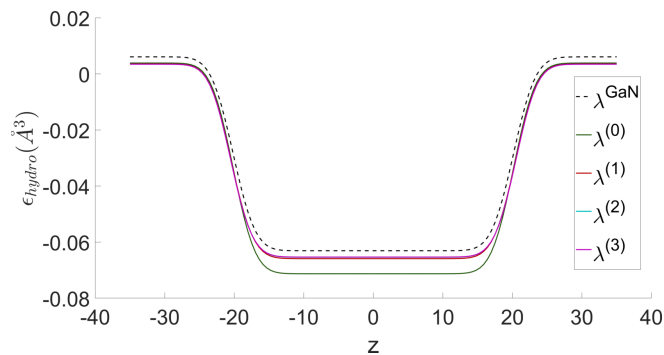


FIG. 3. Hydrostatic strain for increasing correction orders in the elastic constants. Black dashed line is strain assuming uniform elastic constants of the host material  $\lambda^{\text{GaN}}$  while solid lines are for spatially varying elastic constants with correction order  $\lambda^{(N)}$ . As the correction order  $\lambda^{(N)}$  increases, the strain moves toward the uniform case  $\lambda^{\text{GaN}}$ . Note that the lines for  $\lambda^{(2)}$  and  $\lambda^{(3)}$  are overlapping. However, the uniform case  $\lambda^{\text{GaN}}$  underestimates the strain in the dot.

the strain is calculated in its own real space unit cell  $\Omega_s$  with volume  $V_s$ . We denote the strain reciprocal unit cell as  $\Omega_s^{-1}$  such that it contains the wave vectors  $\mathbf{Q}$ , which are defined similarly to Eq. 1 for the electronic cell. Given that strain relaxes more slowly than bound electronic wavefunctions, we only consider  $V_s \geq V_e$ . In this two-unit-cells approximation, the Fourier transform of the strain produced by the quantum dot array is

$$\begin{aligned} \tilde{\epsilon}_{ij}^{\text{a}}(\mathbf{q}) &= \frac{1}{V_s} \sum_{\mathbf{Q} \in \Omega_s^{-1}} \tilde{\epsilon}_{ij}(\mathbf{Q}) \tilde{\chi}_e(\mathbf{q} - \mathbf{Q}) \\ &= \frac{1}{V_s} (\tilde{\epsilon}_{ij} * \tilde{\chi}_e)_s(\mathbf{q}), \end{aligned} \quad (11)$$

where  $\chi_e$  is the characteristic function of the electronic unit cell  $\Omega_e$  in  $\Omega_s$ , which is given for our case in Appendix B. Superscript “a” indicates array. We follow the notation that  $\mathbf{q} \in \Omega_e^{-1}$  and  $\mathbf{Q} \in \Omega_s^{-1}$ .  $(\tilde{\epsilon}_{ij} * \tilde{\chi}_e)_s(\mathbf{q})$  denotes a convolution where the subscript “s” indicates that the convolution is over the wave vectors  $\mathbf{Q} \in \Omega_s^{-1}$ , see Appendix C for Fourier transform and convolution definitions. We show in Sec. III C that choosing the linear dimensions of  $\Omega_s$  to be integer multiples of the linear dimensions of  $\Omega_e$  ensures that all vectors  $\mathbf{q} \in \Omega_e^{-1}$  are also in  $\Omega_s^{-1}$ . This choice allows Eq. 11 to be evaluated efficiently.

### C. Piezoelectric potential

III-nitride materials are strongly piezoelectric, having both spontaneous and strain-driven polarizations [16, 17]. Calculation of the polarization from an electric field requires knowledge of the static dielectric constant  $\varepsilon$  of the material. In prior work, all Fourier-space based approaches assumed a uniform dielectric constant. We present a method to obtain the Fourier transform of the scalar potential  $\tilde{\varphi}(\mathbf{q})$  assuming  $\varepsilon(\mathbf{r})$  changes with the local alloy fraction. We find that correcting for the spatial dependence of the dielectric function leads to important changes in the piezoelectric potential. We also show in Sec. V that this change in piezoelectric potential significantly shifts the lowest quantum dot energy levels. We do not discuss metallic screening, which can be important in highly doped materials [18–20].

Generally, we can write the displacement field  $\mathbf{D}(\mathbf{r})$  as

$$\mathbf{D}(\mathbf{r}) = \varepsilon_0 \mathbf{E}(\mathbf{r}) + \mathbf{P}_{\text{tot}}(\mathbf{r}),$$

where  $\mathbf{E}(\mathbf{r})$  is the electric field,  $\varepsilon_0$  is the vacuum permittivity, and  $\mathbf{P}_{\text{tot}}$  is the total polarization. In the strained material, there are three sources of polarization: bound charge, strain and spontaneous polarization,

$$\mathbf{P}_{\text{tot}}(\mathbf{r}) = \mathbf{P}_{\text{bnd}}(\mathbf{r}) + \mathbf{P}_{\text{st}}(\mathbf{r}) + \mathbf{P}_{\text{sp}}(\mathbf{r}).$$

Here, we assume no free charge screening and so an intrinsic material. Assuming  $\mathbf{P}_{\text{bnd}}$  to be linear with the electric field and incorporated into  $\varepsilon(\mathbf{r})$  as usual,

$$\mathbf{D}(\mathbf{r}) = \varepsilon(\mathbf{r}) \mathbf{E}(\mathbf{r}) + \mathbf{P}_{\text{st}}(\mathbf{r}) + \mathbf{P}_{\text{sp}}(\mathbf{r}), \quad (12)$$

where  $\mathbf{P}_{\text{st}}(\mathbf{r}) + \mathbf{P}_{\text{sp}}(\mathbf{r}) = \mathbf{P}(\mathbf{r})$  is the residual polarization after electric-field induced bound charge has been included in  $\varepsilon(\mathbf{r})$ .

We take  $\varepsilon(\mathbf{r})$  to be  $\varepsilon^{\text{h}}$  in the host material and  $\varepsilon^{\text{d}}$  in the dot material, so

$$\varepsilon(\mathbf{r}) = \varepsilon^{\text{h}} + (\varepsilon^{\text{d}} - \varepsilon^{\text{h}}) \chi_{\text{d}}(\mathbf{r}). \quad (13)$$

We obtain  $\varepsilon^{\text{d}}$  by linear interpolation of the binary compounds' bulk dielectric constants. Taking the divergence of Eq. 12, using  $\nabla \cdot \mathbf{D} = 0$ , taking the Fourier transform and solving for the electric field gives

$$E_m(\mathbf{r}) = -\frac{1}{\varepsilon(\mathbf{r})} \mathcal{F}^{-1} \left\{ \frac{q_n}{q_m} \tilde{P}_n(\mathbf{q}) \right\} \quad (14)$$

where  $\mathcal{F}^{-1}$  represents the inverse Fourier transform. Using  $E_m = -\partial_m \varphi$ , where  $\partial_m \equiv \frac{\partial}{\partial x_m}$  and  $\varphi(\mathbf{r})$  is the scalar potential,

$$\tilde{\varphi}(\mathbf{q}) = -\frac{i}{q_m} \mathcal{F} \left\{ \frac{1}{\varepsilon(\mathbf{r})} \mathcal{F}^{-1} \left\{ \frac{q_n}{q_m} \tilde{P}_n(\mathbf{q}) \right\}(\mathbf{r}) \right\}(\mathbf{q}). \quad (15)$$

For the case of sharp alloy interfaces,  $\chi_{\text{d}}(\mathbf{r})$  is either 1 or 0 and Eq. 13 gives

$$\frac{1}{\varepsilon(\mathbf{r})} = \frac{1}{\varepsilon^{\text{h}}} + \left( \frac{1}{\varepsilon^{\text{d}}} - \frac{1}{\varepsilon^{\text{h}}} \right) \chi_{\text{d}}(\mathbf{r}). \quad (16)$$

We treat the case of smoothly varying alloy fraction in Sec. IV. Putting this result in Eq. 15 gives

$$\tilde{\varphi}(\mathbf{q}) = \tilde{\varphi}_{\text{uni}}^{\text{h}}(\mathbf{q}) + \Delta\tilde{\varphi}(\mathbf{q}) \quad (17)$$

with

$$\tilde{\varphi}_{\text{uni}}^{\text{h}}(\mathbf{q}) = -\frac{i}{q_m} \frac{1}{\varepsilon^{\text{h}}} \frac{q_n}{q_m} \tilde{P}_n(\mathbf{q}) \quad (18)$$

$$\Delta\tilde{\varphi}(\mathbf{q}) = -\frac{i}{q_m} \left( \frac{1}{\varepsilon^{\text{d}}} - \frac{1}{\varepsilon^{\text{h}}} \right) \mathcal{F} \left\{ \chi_{\text{d}}(\mathbf{r}) \mathcal{F}^{-1} \left\{ \frac{q_n}{q_m} \tilde{P}_n(\mathbf{q}) \right\} \right\} \quad (19)$$

Here,  $\tilde{\varphi}_{\text{uni}}^{\text{h}}$  is the contribution to  $\varphi$  with  $\varepsilon_r(\mathbf{r}) = \varepsilon^{\text{h}}$ , and  $\Delta\tilde{\varphi}$  is the change in  $\tilde{\varphi}$  due to the dot material having a different dielectric constant. The polarization fields  $\tilde{P}_n(\mathbf{q})$  for the wurtzite crystal structure are given in terms of strain in Appendix E.

We now show the piezoelectric potentials that result from this formulation, for our model system described in Sec. II A. Figure 4 shows  $\varphi(z)$  along the central axis of the quantum dot calculated with constant  $\varepsilon$  of the dot and host and with Eq. 17. The calculation with spatially varying  $\varepsilon(\mathbf{r})$  agrees with  $\varphi_{\text{uni}}^{\text{d}}$  inside the dot and also agrees with  $\varphi_{\text{uni}}^{\text{h}}$  outside the dot, with a transition near the boundary that is captured by neither of the uniform cases.

We showed in Fig. 3 how spatially varying elastic constants change strain profiles. Figure 5 shows how  $\varphi$  changes due to the elastic constants' correction propagates into the piezoelectric potential. We find that the changes in piezoelectric potential, a peak correction of 8 mV, are significant if looking to converge the energy levels within a few meV's.

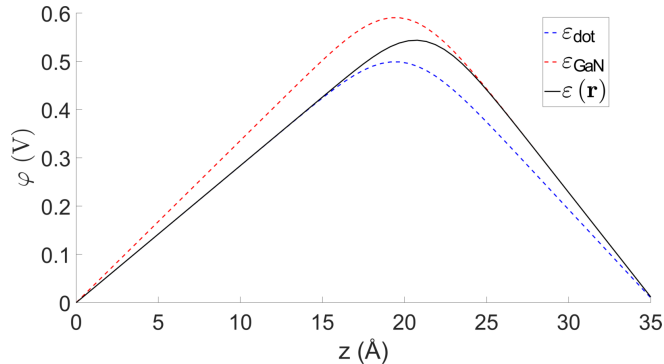


FIG. 4. Piezoelectric potential  $\varphi(z)$  along the central axis, beginning in the center of the dot, with parameters as in Table I. Blue and red dashed lines show  $\varphi$  calculated with uniform  $\varepsilon(\mathbf{r}) = \varepsilon^{\text{h}}$  and  $\varepsilon(\mathbf{r}) = \varepsilon^{\text{d}}$ , respectively. Black line shows the case with spatially varying  $\varepsilon(\mathbf{r})$ . Note that the  $\varphi$  is antisymmetric in  $z$ . These results show that the case of uniform  $\varepsilon$  cannot capture  $\varphi$  throughout the system. Strain calculations include third order corrections for the nonuniform elastic constants.

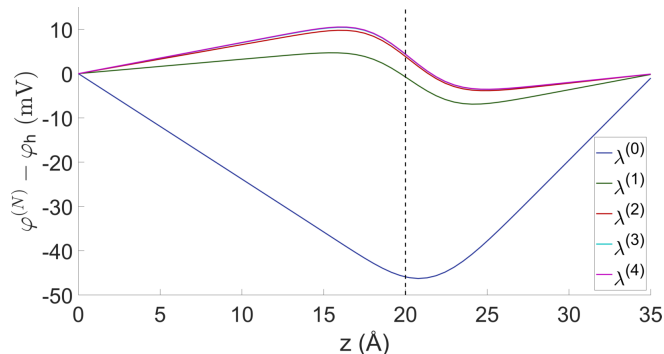


FIG. 5. Piezoelectric potential difference along the central axis of the dot for various elastic constant corrections. Potential difference is with respect to  $\varphi_{\text{h}}(\mathbf{r})$ , which is calculated with a uniform  $\lambda(\mathbf{r}) = \lambda^{\text{GaN}}$ . Calculations implement an alloy smoothing of  $\delta = [1.5, 1.5, 2.5] \text{ \AA}$ , which is described in Sec. IV, and the vertical dashed line indicates the nominal material interface without smoothing. These results are for the same system as Fig. 4, calculated using various orders of correction for the effects of nonuniform elastic constants, described in Sec. II B 1. Spatially varying dielectric constants are included. The zeroth order case (blue line) shows  $\lambda(\mathbf{r}) = \lambda^{\text{d}}$ .

### III. SYMMETRY ADAPTED BASIS $\mathbf{k} \cdot \mathbf{p}$ FOR WURTZITE QUANTUM DOTS

Here, we present the quantum dot  $\mathbf{k} \cdot \mathbf{p}$  model we use for electronic structure calculations. We first present a theory for bulk materials and use it to construct a theory for quantum dots. This quantum dot Hamiltonian is written in a symmetry adapted basis, which reduces the computational cost for calculating and diagonalizing the Hamiltonian. In this symmetry adapted basis, we show how the strain produced by the quantum dots contributes to the Hamiltonian. We also introduce strain effects using a different unit cell than that of the electronic cell defined in Fig. 1. In this section, our goal is to show our method of efficiently including strain in the quantum dot  $\mathbf{k} \cdot \mathbf{p}$  model, which we do by choosing the strain unit cell's dimensions to be integer multiples of the unit cell used for the electronic structure calculations.



### A. Bulk $\mathbf{k} \cdot \mathbf{p}$ model

To describe the electronic structure of bulk wurtzite systems, we use an 8-band  $\mathbf{k} \cdot \mathbf{p}$  model, which includes spin-orbit coupling, crystal field splitting and strain. An 8-band  $\mathbf{k} \cdot \mathbf{p}$  model for bulk wurtzite material has been presented by Ref. [7] in the basis of  $\Gamma$ -point Bloch functions. References [7, 21] presented a 6-band model using eigenfunctions of the angular momentum operator  $\hat{J}_z$ . Since choosing  $\hat{J}_z$  eigenfunctions aids in the construction of a symmetry adapted basis, which is presented in Sec. III B, we have used these two references to construct an 8-band Hamiltonian in the  $\hat{J}_z$  eigenfunctions basis. More precisely, we have constructed the Hamiltonian using  $S$ ,  $X$ ,  $Y$  and  $Z$   $\Gamma$ -point Bloch functions as a basis and then performed a basis transformation to obtain the  $\hat{J}_z$  eigenfunctions basis. While  $\mathbf{k} \cdot \mathbf{p}$  parameters are usually obtained in  $S$ ,  $X$ ,  $Y$  and  $Z$  basis, recent work has obtained  $\mathbf{k} \cdot \mathbf{p}$  parameters directly in the symmetry adapted basis using *ab initio* calculations [22].

We consider the time-independent Schrödinger equation for a single electron

$$\hat{H}|\psi\rangle = E|\psi\rangle \quad (20)$$

where

$$\hat{H} = \hat{K} + \hat{V} + \hat{H}_{\text{so}} + \hat{H}_{\text{cr}} + \hat{H}_{\text{st}} \quad (21)$$

Here,  $\hat{K}$  is the kinetic term of the electrons,  $\hat{V}$  the potential from the electron-ion interaction,  $\hat{H}_{\text{so}}$  is spin-orbit coupling,  $\hat{H}_{\text{cr}}$  is crystal field splitting and  $\hat{H}_{\text{st}}$  is strain coupling. We expand  $|\psi\rangle$  in terms of the  $\hat{J}_z$  eigenfunctions  $|u_i\rangle$

$$|\psi\rangle = e^{i\mathbf{k}\cdot\mathbf{r}} \sum_{\alpha=1}^8 C_{\alpha} |u_i\rangle \quad (22)$$

where

$$\begin{aligned} |u_1\rangle &= |iS, \uparrow\rangle & |u_5\rangle &= |-iS, \downarrow\rangle \\ |u_2\rangle &= \left| -\frac{X+iY}{\sqrt{2}}, \uparrow \right\rangle & |u_6\rangle &= \left| \frac{X-iY}{\sqrt{2}}, \downarrow \right\rangle \\ |u_3\rangle &= \left| \frac{X-iY}{\sqrt{2}}, \uparrow \right\rangle & |u_7\rangle &= \left| -\frac{X+iY}{\sqrt{2}}, \downarrow \right\rangle \\ |u_4\rangle &= |Z, \uparrow\rangle & |u_8\rangle &= |Z, \downarrow\rangle \end{aligned} \quad (23)$$

Here,  $S$ ,  $X$ ,  $Y$  and  $Z$  are  $\Gamma$ -point Bloch functions with arrows indicating spin. The eigenvalues of the  $\hat{J}_z$  eigenfunctions are

$$J_z = \left\{ \frac{1}{2}, \frac{3}{2}, -\frac{1}{2}, \frac{1}{2}, -\frac{1}{2}, -\frac{3}{2}, \frac{1}{2}, -\frac{1}{2} \right\},$$

respectively. Inserting Eq. 22 into 20, the eigenvalue problem can be written as

$$H_{\alpha'\alpha} C_{\alpha} = E C_{\alpha'} \quad (24)$$

Keeping terms only up to order  $k^2$ , the 8x8  $\mathbf{k} \cdot \mathbf{p}$  Hamiltonian is

$$H = \begin{bmatrix} g(\mathbf{k}) & \gamma \\ -\gamma^* & g^*(\mathbf{k}) \end{bmatrix} \quad (25)$$

where

$$g(\mathbf{k}) = g_1(\mathbf{k}) + g_2(\mathbf{k}) + g_{\text{cr}} + g_{\text{so}} + g_{\text{st}}$$

$$g_1(\mathbf{k}) = \begin{bmatrix} E'_c & -\frac{P_2}{\sqrt{2}}k_+ & \frac{P_2}{\sqrt{2}}k_- & P_1k_z \\ -\frac{P_2}{\sqrt{2}}k_- & E'_v & 0 & 0 \\ \frac{P_2}{\sqrt{2}}k_+ & 0 & E'_v & 0 \\ P_1k_z & 0 & 0 & E'_v \end{bmatrix}$$

$$\begin{aligned}
g_2(\mathbf{k}) &= \begin{bmatrix} A'_2(k_x^2 + k_y^2) + A'_1 k_z^2 & 0 & 0 & 0 \\ 0 & \left(\frac{L'_1 + M_1}{2}\right)(k_x^2 + k_y^2) + M_2 k_z^2 & -\frac{1}{2} N'_1 k_-^2 & -\frac{1}{\sqrt{2}} N'_2 k_- k_z \\ 0 & -\frac{1}{2} N'_1 k_+^2 & \left(\frac{L'_1 + M_1}{2}\right)(k_x^2 + k_y^2) + M_2 k_z^2 & \frac{1}{\sqrt{2}} N'_2 k_+ k_z \\ 0 & -\frac{1}{\sqrt{2}} N'_2 k_+ k_z & \frac{1}{\sqrt{2}} N'_2 k_- k_z & M_3(k_x^2 + k_y^2) + L'_2 k_z^2 \end{bmatrix} \\
g_{\text{st}} &= \begin{bmatrix} a_2(\epsilon_{xx} + \epsilon_{yy}) + a_1 \epsilon_{zz} & 0 & 0 & 0 \\ 0 & \frac{1}{2}(l_1 + m_1)(\epsilon_{xx} + \epsilon_{yy}) + m_2 \epsilon_{zz} & -\frac{1}{2}(l_1 - m_1)(\epsilon_{xx} - \epsilon_{yy}) + i n_1 \epsilon_{xy} & -\frac{n_2(\epsilon_{xz} - i \epsilon_{yz})}{\sqrt{2}} \\ 0 & -\frac{1}{2}(l_1 - m_1)(\epsilon_{xx} - \epsilon_{yy}) - i n_1 \epsilon_{xy} & \frac{1}{2}(l_1 + m_1)(\epsilon_{xx} + \epsilon_{yy}) + m_2 \epsilon_{zz} & \frac{n_2(\epsilon_{xz} + i \epsilon_{yz})}{\sqrt{2}} \\ 0 & -\frac{n_2(\epsilon_{xz} + i \epsilon_{yz})}{\sqrt{2}} & \frac{n_2(\epsilon_{xz} - i \epsilon_{yz})}{\sqrt{2}} & m_3(\epsilon_{xx} + \epsilon_{yy}) + l_2 \epsilon_{zz} \end{bmatrix} \quad (26)
\end{aligned}$$

$$g_{\text{cr}} = \Delta_{\text{cr}} \begin{bmatrix} 0 & 0 & 0 & 0 \\ 0 & 1 & 0 & 0 \\ 0 & 0 & 1 & 0 \\ 0 & 0 & 0 & 0 \end{bmatrix}$$

$$g_{\text{so}} = \frac{\Delta_{\text{so}}}{3} \begin{bmatrix} 0 & 0 & 0 & 0 \\ 0 & 1 & 0 & 0 \\ 0 & 0 & -1 & 0 \\ 0 & 0 & 0 & 0 \end{bmatrix}$$

$$\gamma = \frac{\sqrt{2} \Delta_{\text{so}}}{3} \begin{bmatrix} 0 & 0 & 0 & 0 \\ 0 & 0 & 0 & 0 \\ 0 & 0 & 0 & 1 \\ 0 & 0 & -1 & 0 \end{bmatrix}$$

Here,  $\Delta_{\text{cr}}$  and  $\Delta_{\text{so}}$  are the crystal field splitting and spin-orbit coupling, respectively. The band edges are  $E'_c = E_v + E_g + \Delta_{\text{cr}} + \frac{\Delta_{\text{so}}}{3} + \varphi$  and  $E'_v = E_v + \varphi$  where  $\varphi$  is any additional scalar potential such as the piezoelectric potential. The  $A'_i$  parameters are related to the Kane parameters  $P_i$  and  $L'_i, M_i, N'_i$  to the Luttinger-like parameters  $A_i$ , all of which are shown in Appendix A.  $g_{\text{st}}$  is the contribution to the Hamiltonian due to strain  $\epsilon_{ij}$ . The parameters  $a_i, l_i, m_i$  and  $n_i$  for the strain contribution are given in Appendix A in terms of deformation potentials.

In example calculations, alloy parameters have been obtained by linearly interpolating between bulk GaN and InN parameters, which are given in Appendix A, except the band gap, which has bowing included.

## B. Quantum dot $\mathbf{k} \cdot \mathbf{p}$

For the quantum dot system, we construct the Hamiltonian from the bulk system described in Section III A. We use slowly varying envelope functions and apply a spatial dependence to the bulk Hamiltonian. The problem is expressed in a symmetry adapted basis to obtain a block diagonal Hamiltonian from which we calculate the eigenstates of the quantum dot.

We start from Eq. 20, but expand  $|\psi\rangle$  in terms of envelope functions  $F_\alpha(\mathbf{r})$  that are slowly varying compared to the lattice constant [8, 9, 11, 23],

$$|\psi\rangle = \sum_{\alpha=1}^8 |F, \alpha\rangle$$

$$\langle \mathbf{r} | F, \alpha \rangle = F_\alpha(\mathbf{r}) u_\alpha(\mathbf{r}) \quad (27)$$

where the  $u_\alpha(\mathbf{r})$  are defined by Eq. 23 and are periodic with the crystal lattice. Analogous to Eq. 24, this envelope function expansion leads to

$$\sum_{\alpha=1}^8 H_{\alpha'\alpha} F_\beta(\mathbf{r}) = E F_{\alpha'}(\mathbf{r}) \quad (28)$$

where  $H_{\alpha'\alpha}$  are the bulk Hamiltonian matrix elements from Eq. 25. Due to the broken translation symmetry in the quantum dot system, we apply the substitution

$$k_j \rightarrow -i \frac{\partial}{\partial x_j} \quad (29)$$

to the bulk Hamiltonian in Eq. 25. Each parameter in the bulk Hamiltonian also has a spatial dependence based on the alloy distribution,

$$f(\mathbf{r}) = f^d \chi_d(\mathbf{r}) + f^h [1 - \chi_d(\mathbf{r})] \quad (30)$$

Here,  $f$  stands for any of the parameters in the bulk Hamiltonian that are material dependent.  $f^h$  and  $f^d$  are the parameter values of the host and alloyed dot material, respectively. Applying the substitution in Eq. 29 to Eq. 25, the Hamiltonian consists of terms of the form  $f(\mathbf{r})$ ,  $f(\mathbf{r}) \frac{\partial}{\partial x_j}$  and  $f(\mathbf{r}) \frac{\partial^2}{\partial x_i \partial x_j}$ . To preserve Hermiticity, we symmetrize the derivatives [9, 23, 24]:

$$f(\mathbf{r}) \frac{\partial}{\partial x_j} \rightarrow \frac{1}{2} \left( f(\mathbf{r}) \frac{\partial}{\partial x_j} + \frac{\partial}{\partial x_j} f(\mathbf{r}) \right) \quad (31)$$

$$f(\mathbf{r}) \frac{\partial^2}{\partial x_i \partial x_j} \rightarrow \frac{1}{2} \left( \frac{\partial}{\partial x_i} f(\mathbf{r}) \frac{\partial}{\partial x_j} + \frac{\partial}{\partial x_j} f(\mathbf{r}) \frac{\partial}{\partial x_i} \right) \quad (32)$$

The envelope functions  $F_\alpha(\mathbf{r})$  are periodic with the superlattice and can be expanded in Fourier domain using the superlattice reciprocal wave vectors  $\mathbf{q}$  defined in Eq. 1. Writing the envelope functions  $F_\alpha(\mathbf{r})$  in terms of plane waves leads to a non-sparse Hamiltonian [8, 23]. For computational efficiency, we use a symmetry adapted basis, which takes advantage of the  $C_6$  symmetry of the wurtzite crystal structure by block diagonalizing the Hamiltonian. Symmetry adapted bases have been fully described for both zincblende and wurtzite systems [9, 10]. We use a symmetry-adapted basis with elements  $|m_f, \alpha, \mathbf{q}\rangle$  where  $\mathbf{q} = (q_x, q_y, q_z)$  are chosen within a single sextant, so  $0 \leq q_y \leq \tan(\frac{2\pi}{6}) q_x$ , and  $m_f = \{-5/2, -3/2, -1/2, 1/2, 3/2, 5/2\}$  can be interpreted as a total quasi angular momentum [10, 11]. This basis consists of the basis functions of the irreducible representations of the double group  $\bar{C}_6$ . Using this basis reduces the Fourier space sampling to a single sextant of the full space and block diagonalizes the Hamiltonian into 6 blocks, which are labeled by  $m_f$ . This block diagonalization greatly reduces the computational cost to diagonalize the Hamiltonian. Figure 6 shows an example of the Fourier space sampling used in the symmetry adapted basis. Written out, the basis states are

$$|m_f, \alpha, \mathbf{q}\rangle = \Lambda(m_f, \alpha, \mathbf{q}, \mathbf{r}) |u_\alpha\rangle \quad (33)$$

$$\Lambda(m_f, \alpha, \mathbf{q}, \mathbf{r}) = \begin{cases} \frac{1}{\sqrt{6}} \sum_{l=0}^5 e^{i(\vec{\mathbf{R}}_l \mathbf{q}) \cdot \mathbf{r}} e^{il \frac{2\pi}{6} [m_f - J_z(\alpha)]} & q_x \neq 0 \text{ or } q_y \neq 0 \\ e^{i\mathbf{q} \cdot \mathbf{r}} & q_x = q_y = 0 \quad J_z(\alpha) = m_f \end{cases} \quad (34)$$

where  $\vec{\mathbf{R}}_l$  is the  $l \frac{2\pi}{6}$  rotation around the z-axis. Equation 34 distinguishes wave vectors that are purely along the z-axis from those that have an xy-component, which we denote by  $\mathbf{q}_z$  and  $\mathbf{q}$ , respectively. These two cases differ because a z-axis rotation leaves  $\mathbf{q}_z$  invariant while sending  $\mathbf{q}$  to a new wave vector  $\vec{\mathbf{R}}_l \mathbf{q}$ . The case of  $|m_f, \alpha, \mathbf{q}_z\rangle$  with  $J_z(\alpha) \neq m_f$  does not exist in the basis set. Using the symmetry adapted basis, the eigenstates can be written

$$|\psi_{i, m_f}\rangle = \sum_{\alpha=1}^8 \sum_{\mathbf{q}} A_{i m_f}^\alpha(\mathbf{q}) |m_f, \alpha, \mathbf{q}\rangle \quad (35)$$

where the  $\mathbf{q}$  summation is restricted to the sextant, shown in Fig. 6.

Writing the envelope functions in the symmetry adapted basis, the eigenvalue problem in Eq. 28 can then be written

$$\sum_{\alpha=1}^8 \sum_{\mathbf{q}} \mathcal{H}_{m_f \alpha' \alpha}(\mathbf{q}', \mathbf{q}) A_{im_f}^{\alpha}(\mathbf{q}) = E_i A_{im_f}^{\alpha'}(\mathbf{q}') \quad (36)$$

with

$$\begin{aligned} \mathcal{H}_{m_f \alpha' \alpha}(\mathbf{q}', \mathbf{q}) &\equiv \langle m_f, \alpha', \mathbf{q}' | \hat{\mathcal{H}} | m_f, \alpha, \mathbf{q} \rangle \\ &= \frac{1}{V_e} \int_{V_e} d^3 \mathbf{r} \Lambda^*(\mathbf{r}) H_{\alpha' \alpha}(\mathbf{r}) \end{aligned} \quad (37)$$

where  $H_{\alpha' \alpha}$  are the bulk Hamiltonian matrix elements presented in Sec. III A. Expressions for  $\mathcal{H}_{m_f \alpha' \alpha}(\mathbf{q}', \mathbf{q})$  are fully written out in Appendix F in terms of the bulk Hamiltonian matrix elements and quantum dot characteristic function.

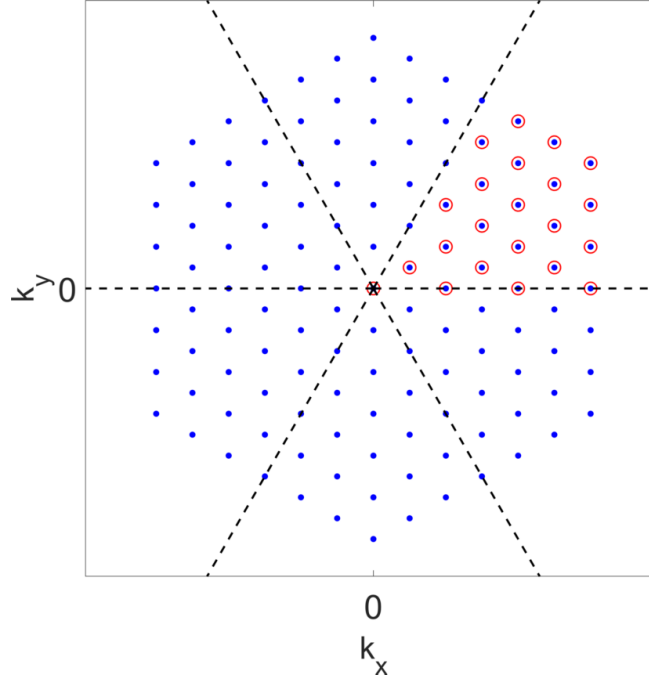


FIG. 6. Fourier space sampling used for the symmetry adapted basis. Red circles are the Fourier space points  $\mathbf{q}$  used in the symmetry adapted basis. Blue dots are the full Fourier space sampled by rotations  $\hat{\mathbf{R}}_l \mathbf{q}$ . Dashed lines highlight the 6 sextants.

### C. Including strain and piezoelectric effects

Deformation potentials and piezoelectric effects, which are both strain-driven, are important for accurate calculations of electronic structure in III-N materials. However, including deformation potentials can be computationally costly for the case of isolated dots. The two-unit cell approach presented in Sec. II B 2 allows for the study of isolated dots, but at the cost of computationally expensive convolutions. Additionally, another layer of convolutions appears in the Hamiltonian matrix elements, leading to composed convolutions. Here, we present the matrix elements due to strain and show our computationally efficient approach of dealing with these composed convolutions by choosing the linear dimensions of the real-space strain cell  $\Omega_s$  to be integer multiples of those of the electronic cell  $\Omega_e$ .

The bulk strain Hamiltonian matrix elements in Eqs. 25 and 26 can be written as

$$H_{\alpha' \alpha} = \sum_{ij} f_{\alpha' \alpha}^{ij} \epsilon_{ij}(\mathbf{r})$$

where the  $f_{\alpha' \alpha}^{ij}$  consist of  $\mathbf{k} \cdot \mathbf{p}$  parameters ( $a_i$ ,  $l_i$ ,  $m_i$  and  $n_i$ ). Using the prescription of Sec. III B, the strain contributions to the quantum dot Hamiltonian are

$$\mathcal{H}_{m_f \alpha' \alpha}^{ij, \text{st}}(\mathbf{q}', \mathbf{q}) = \frac{1}{6} \sum_{l'=0}^5 \sum_{l=0}^5 e^{i \frac{2\pi}{6} \{l[m_f - J_z(\alpha)] - l'[m_f - J_z(\alpha')]\}} h_{\alpha' \alpha}^{ij, \text{st}}(\overleftarrow{\mathbf{R}}_{l'} \mathbf{q}', \overleftarrow{\mathbf{R}}_l \mathbf{q})$$

$$\mathcal{H}_{m_f \alpha' \alpha}^{ij, \text{st}}(\mathbf{q}', \mathbf{q}_z) = \frac{1}{\sqrt{6}} \sum_{l'=0}^5 e^{-il' \phi[m_f - J_z(\alpha')]} h_{\alpha' \alpha}^{ij, \text{st}}(\overleftarrow{\mathbf{R}}_{l'} \mathbf{q}', \mathbf{q}_z)$$

$$\mathcal{H}_{m_f \alpha' \alpha}^{ij, \text{st}}(\mathbf{q}_z, \mathbf{q}_z) = h_{\alpha' \alpha}^{ij, \text{st}}(\mathbf{q}_z, \mathbf{q}_z)$$

where

$$h_{\alpha' \alpha}^{ij, \text{st}}(\mathbf{q}', \mathbf{q}) = \frac{(2\pi)^3 f_{\alpha' \alpha}^{ij, \text{h}}}{V_e} \tilde{\epsilon}_{ij}^a(\mathbf{q}' - \mathbf{q}) + \frac{(2\pi)^6 (f_{\alpha' \alpha}^{ij, \text{d}} - f_{\alpha' \alpha}^{ij, \text{h}})}{V_e^2} (\tilde{\chi}_d * \tilde{\epsilon}_{ij}^a)_e(\mathbf{q}' - \mathbf{q}). \quad (38)$$

Here,  $f_{\alpha' \alpha}^{ij, \text{h}}$  and  $f_{\alpha' \alpha}^{ij, \text{d}}$  are the  $\mathbf{k} \cdot \mathbf{p}$  parameters for bulk host and dot materials, respectively.  $\tilde{\epsilon}_{ij}^a$  is the strain produced by the quantum dot array calculated in Sec. II B. The subscript “e” in  $(\tilde{\chi}_d * \tilde{\epsilon}_{ij}^a)_e$  indicates that the convolution is over the wave vectors  $\mathbf{q} \in \Omega_e^{-1}$ . Inserting the superlattice strain from Eq. 11 into the  $\mathbf{k} \cdot \mathbf{p}$  strain matrix elements from Eq. 38 leads to composed convolutions,

$$(\tilde{\chi}_d * \tilde{\epsilon}_{ij}^a)_e(\mathbf{q}) = \sum_{\mathbf{q}' \in \Omega_e^{-1}} \tilde{\chi}_d(\mathbf{q}') \tilde{\epsilon}_{ij}^a(\mathbf{q} - \mathbf{q}') \quad (39)$$

$$= \frac{1}{V_s} \sum_{\mathbf{q}' \in \Omega_e^{-1}} \tilde{\chi}_d(\mathbf{q}') \sum_{\mathbf{Q} \in \Omega_s^{-1}} \tilde{\epsilon}_{ij}(\mathbf{Q}) \tilde{\chi}_e(\mathbf{q} - \mathbf{q}' - \mathbf{Q}) \quad (40)$$

which can be computationally demanding depending on the number of wave vectors used. The original proposal of using a large strain cell with a smaller electronic cell imposed no relationship between their sizes [11]. Equation 40 then requires evaluating  $\tilde{\chi}_e$  at points  $\mathbf{q} - \mathbf{q}' - \mathbf{Q}$ , which are contained on neither the electronic nor strain meshes, requiring a unique convolution be calculated for every  $\mathbf{q}'$ . It is well known that using the convolution theorem to compute a convolution between two vectors of length  $N$  has a computational cost that scales as  $N \log(N)$ . Similarly, the computational cost for a convolution on a 3D  $N \times N \times N$  mesh scales as  $N^3 \log(N)$ . Computing the composed convolutions in Eq. 40 would then scale as  $N_e^3 \log(N_e) N_s^3 \log(N_s)$  since a convolution in  $\mathbf{Q}$  has to be calculated for each individual  $\mathbf{q}'$ . Note that the convolutions from Eqs. 39-40 are linear convolutions, which implies that the arrays of function values must be padded with zeros before using the convolution theorem as detailed in Appendix C. This zero padding increases both  $N_e$  and  $N_s$ . We show that choosing a strain unit cell to be a supercell of the electronic unit cell reduces the number of convolutions to compute, leading to an improved scaling of  $N_e^3 \log(N_e) + N_s^3 \log(N_s)$ .

Choosing the strain unit cell linear dimensions to be multiples of the electronic cell, we have

$$L_i^s = n_i L_i^e \quad i = 1, 2, 3 \quad (41)$$

where the  $n_i$  take positive integer values. This choice of real-space unit cells leads to the electronic Fourier-space mesh being contained in the strain mesh  $\Omega_e^{-1} \subset \Omega_s^{-1}$ . The wave vectors  $\mathbf{Q}$  then have a spacing that is a fraction of the spacing of the electronic wave vectors  $\mathbf{q}$ ,

$$\Delta Q_i = \frac{\Delta q_i}{n_i} \quad (42)$$

Note that from Eq. 39,  $\tilde{\epsilon}_{ij}^a$  is only sampled at points  $\Delta \mathbf{q} = \mathbf{q} - \mathbf{q}'$ , which belong to the electronic mesh. Our procedure starts with using the convolution theorem (see Appendix C) to efficiently calculate the inner convolution  $(\tilde{\epsilon}_{ij} * \tilde{\chi}_e)_s(\mathbf{Q})$  on the strain mesh to obtain  $\tilde{\epsilon}_{ij}^a(\mathbf{Q})$ . Since the wave vectors  $\mathbf{Q}$  also contain the wave vectors  $\mathbf{q}$ , we can then extract the points that lie on the electronic mesh to obtain  $\tilde{\epsilon}_{ij}^a(\mathbf{q})$ . Lastly, we perform the second convolution  $(\tilde{\chi}_d * \tilde{\epsilon}_{ij}^a)_e(\mathbf{q})$ , again utilizing the convolution theorem. This workflow is shown in Fig. 8(a). In our method, we compute only two 3D convolutions and so get a complexity scaling of  $N_e^3 \log(N_e) + N_s^3 \log(N_s)$ , which is a considerable improvement compared to the non-overlapping case. Note that  $N_s$  is generally much larger than  $N_e$  to obtain appropriate convergence, so the computational cost is dominated by the convolutions on  $\Omega_s^{-1}$ .

The piezoelectric potential brings no additional complexity, and the workflow for calculating the piezoelectric potential is shown in Fig. 8(b). The potential is initially calculated on the strain mesh, and the electronic mesh portion is extracted to calculate the piezoelectric potential contributions to the Hamiltonian, which are written out in Appendix F.

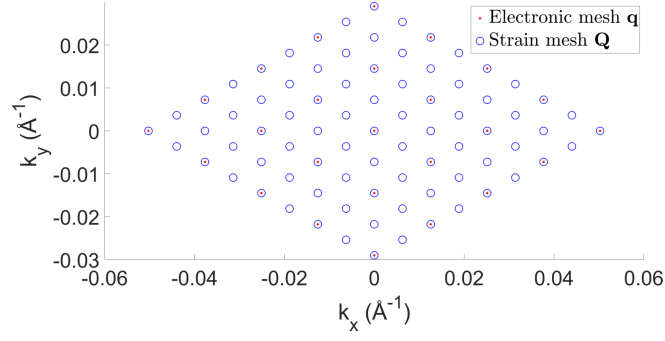


FIG. 7. Example of Fourier space meshes where  $n_{12} = 2$ , leading to  $\Delta Q_i = \frac{\Delta q_i}{2}$ , which implies the vectors  $\mathbf{Q}$  contain all the vectors  $\mathbf{q}$ .

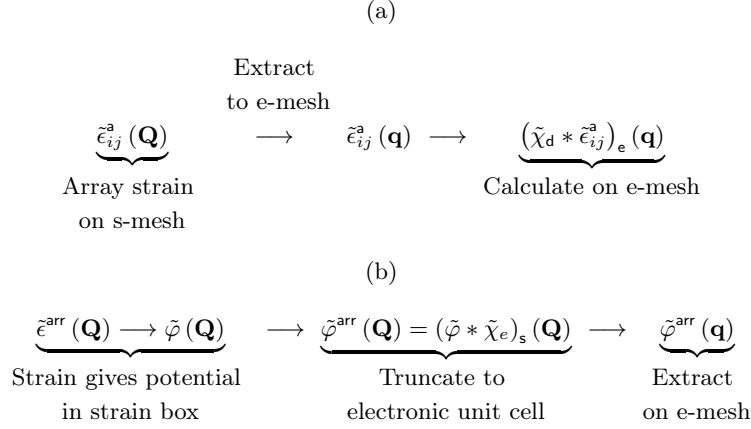


FIG. 8. (a) Workflow for calculation of composed convolutions of the form shown in Eq. 39. (b) Workflow used to obtain piezoelectric potential on the electronic mesh from the strain on the strain mesh. e-mesh and s-mesh signify the Fourier space electronic and strain meshes, respectively.

#### IV. SMOOTH ALLOY PROFILE

When InGaN devices are grown by molecular beam epitaxy (MBE), indium diffuses between layers [1]. While most studies of MBE-grown materials simulate abrupt junctions, this diffusion leads to smoothing of the material interfaces, producing a continuously varying alloy fraction, which changes the local band properties and lattice constant, which in turn change strain and polarization fields. This smooth alloy profile must be included for accurate modeling. Smooth indium profiles also provide a computational benefit, since sharp features of the confining potentials are removed, so fewer wave vectors are required to attain convergence. In this section, we present a method to include alloy diffusion effects by effectively smoothing the characteristic function of the dot. We focus on indium alloying here for the examples, but the methods are general for all  $\mathbf{k} \cdot \mathbf{p}$  calculations of alloy structures.

##### 1. Smoothing method

In the case of a sharp material interface, the local alloy fraction  $X(\mathbf{r})$  can be defined by the characteristic function of the dot

$$X(\mathbf{r}) = X_0 \chi_d(\mathbf{r}),$$

where the characteristic function  $\chi_d(\mathbf{r})$  defines the geometry of the dot with indium fraction  $X_0$ . By convolving with a Gaussian  $G(\mathbf{r}, \boldsymbol{\delta}) = \frac{1}{\sqrt{2\pi\delta_x\delta_y\delta_z}} e^{-\frac{1}{2}\left(\frac{x^2}{\delta_x^2} + \frac{y^2}{\delta_y^2} + \frac{z^2}{\delta_z^2}\right)}$  or other kernel, we can obtain a smooth version of the characteristic

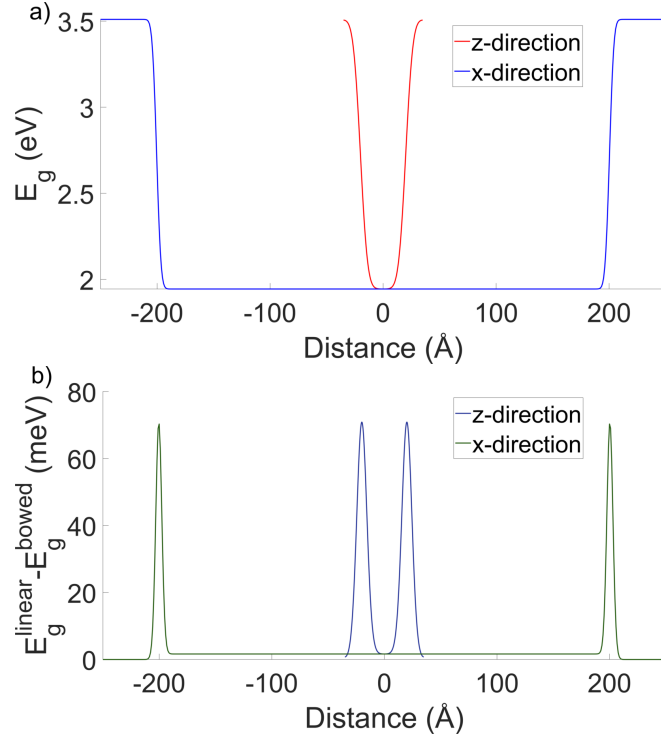


FIG. 9. (a) Band gap in a quantum dot system obtained by bowed interpolation using Eq. 46 along the z and y axes through the center of the dot. Band gap obtained from linear interpolation using Eq. 47 is visually indistinguishable. (b) Difference of the bowed and linearly interpolated band gaps along the z and x axes. Quantum dot parameters are listed in Table I. However, for computational simplicity and smooth curves, these results were obtained using a rectangular real-space unit cell with dimensions  $L_x = L_y = 500\text{\AA}$  and  $L_z = 70\text{\AA}$  and a smoothing of  $\delta = [3, 3, 5]\text{\AA}$ .

function

$$\begin{aligned} X_{\text{sm}}(\mathbf{r}) &= (X_0 \chi_d * G)(\mathbf{r}) \\ &= X_0 \chi_{\text{sm}}(\mathbf{r}), \end{aligned}$$

where  $\boldsymbol{\delta} = [\delta_x, \delta_y, \delta_z]$  controls the radius of smoothing and needs to be chosen to model the desired alloy diffusion.  $G(\mathbf{r}, \boldsymbol{\delta})$  is normalized to preserve the total amount of alloying element, and  $\chi_{\text{sm}}(\mathbf{r})$  is a smoothed characteristic function. Using the convolution theorem, the smoothed characteristic function satisfies

$$\tilde{\chi}_{\text{sm}}(\mathbf{q}) = \tilde{\chi}_d(\mathbf{q}) e^{-\frac{(\delta_x^2 q_x^2 + \delta_y^2 q_y^2 + \delta_z^2 q_z^2)}{2}}.$$

Note that  $\chi_{\text{sm}}(\mathbf{r})$  is no longer strictly a characteristic function, as it takes values continuously between 0 and 1. We now show that it can be inserted in place of the characteristic function in the previous sections to give  $\mathbf{k} \cdot \mathbf{p}$  parameters, strain and piezoelectric fields accurately with a smooth alloy profile.

## 2. Material parameters

We now focus on the case of InGa<sub>N</sub> to illustrate the interpolation of material parameters. In the case of sharp material interfaces, the host and dot regions each consist of uniform material. The host material is a binary material and has well-defined parameters. The dot region consists of alloyed InGa<sub>N</sub>, and its parameters are obtained by either linear or bowed interpolation of bulk GaN and InN parameters, which are listed in Appendix A.

In the case of a smooth alloy profile, the dot and host regions are no longer uniform, giving the material parameters a smooth spatial dependence. Parameters that were linearly interpolated in the sharp interface case can still be obtained from a simple linear interpolation based on the local alloy fraction  $X(\mathbf{r})$ . The band gap  $E_g$  is nonlinear in the alloy fraction due to a bowing factor. This nonlinearity prevents us from using the convolution theorem in calculating the

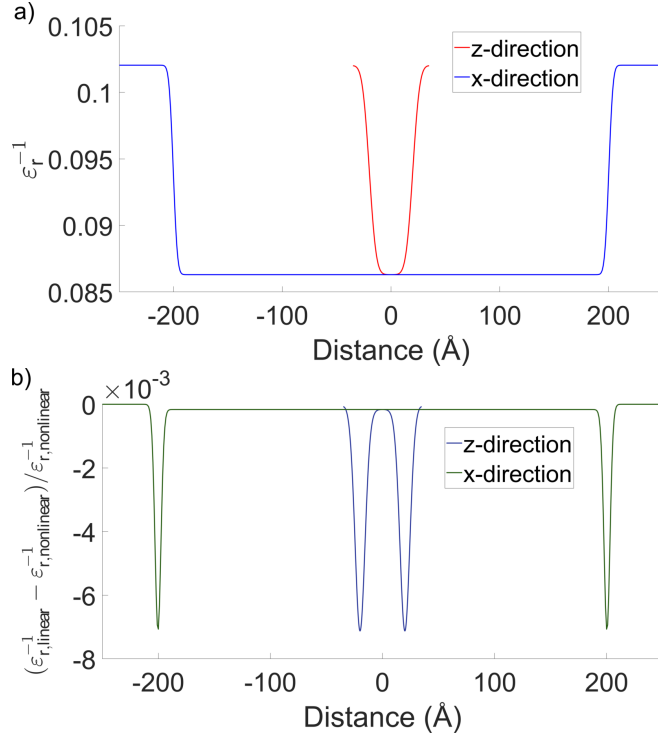


FIG. 10. (a) Inverse dielectric constant from Eq. 48 along the z and x axes through the center of the dot. Linearly interpolated inverse from Eq. 49 is visually indistinguishable. (b) Relative difference of the linear and nonlinear dielectric constants along the z and x axes. Quantum dot parameters are listed in Table I. However, for computational simplicity and smooth curves, these results were obtained using a rectangular real-space unit cell with dimensions  $L_x = L_y = 500\text{\AA}$  and  $L_z = 70\text{\AA}$  and a smoothing of  $\delta = [3, 3, 5]\text{\AA}$ .

Hamiltonian matrix elements. However, we show that neglecting the bowing parameters in the alloy-smoothing region can still give computationally efficient and accurate smoothed profiles when the alloy fraction is not too large.

The local value for any of the linearly interpolated material parameters depends on the local alloy fraction

$$f(\mathbf{r}) = f^B X(\mathbf{r}) + [1 - X(\mathbf{r}, X_0)] f^A \quad (43)$$

where  $f$  can be a parameter such as lattice constant, and subscripts A and B stand for the two binary materials, GaN and InN for example. For this case of linearly interpolated quantities, smoothed parameters can be written:

$$f(\mathbf{r}) = f^d(X_0) \chi_{sm}(\mathbf{r}) + [1 - \chi_{sm}(\mathbf{r})] f^A \quad (44)$$

where  $f^d(X_0)$  is the linearly interpolated material parameter at the nominal alloy fraction  $X_0$  of the quantum dot.

Band gaps do not vary linearly with alloy fraction and are generally well described with a bowing term, as

$$E_g(\mathbf{r}) = E_g^B X(\mathbf{r}) + [1 - X(\mathbf{r})] E_g^A - X(\mathbf{r}) [1 - X(\mathbf{r}, X_0)] C \quad (45)$$

where  $C$  is a bowing constant. Following the same procedure as in Eq. 44, a smoothed version can be written:

$$\begin{aligned} E_g(\mathbf{r}) &= X_0 \chi_{sm}(\mathbf{r}) E_g^B + [1 - X_0 \chi_{sm}(\mathbf{r})] E_g^A - C X_0 \chi_{sm}(\mathbf{r}) [1 - X_0 \chi_{sm}(\mathbf{r})] \\ &= E_g^A + [E_g^B - E_g^A] E_g^A X_0 \chi_{sm}(\mathbf{r}) - C X_0 \chi_{sm}(\mathbf{r}) [1 - X_0 \chi_{sm}(\mathbf{r})] \end{aligned} \quad (46)$$

where the first two terms are the linear interpolation and the last term is the bowing. This bowing term brings additional complexity when performing  $\mathbf{k} \cdot \mathbf{p}$  calculations due to the nonlinearity in  $\chi_{sm}(\mathbf{r})$ . We approximate the band gap by a linear interpolation between the host and dot band gaps,

$$E_g(\mathbf{r}) \approx E_g^d(X_0) \chi_{sm}(\mathbf{r}) + [1 - \chi_{sm}(\mathbf{r})] E_g^h. \quad (47)$$

Here,  $E_g^d$  is the bulk band gap at an alloy fraction of  $X_0$  and  $E_g^h$  is the bulk band gap of the host material. This linear interpolation gives a good approximation for the band gap for most regions and as well for moderate indium fractions, as shown in Fig. 9. The regions with largest deviation are in the same locations where  $E_g$  changes over 1.5 eV, so we expect the slight shift of position where each band gap value occurs to have minimal effect. The neglect of the  $\chi_{sm}^2$  term allows the theory to stay linear and therefore efficiently calculated with the convolution theorem.



### 3. Strain and the piezoelectric potential

Here we show how smoothing is included in the strain and piezoelectric potential calculations. Once calculated, those strains and piezoelectric potentials can be included in the  $\mathbf{k} \cdot \mathbf{p}$  model exactly as shown in Sec. III C.

Following the derivations from Refs. [8, 13], it is not obvious how smoothing is to be implemented in strain calculations since they begin from the stress of the sharp interface dot/barrier interface. However, Ref. [15] presents an alternative derivation for the same strain calculation indicating that  $\chi(\mathbf{r})$  in the strain expressions can be exchanged for the smoothed version  $\chi_{\text{sm}}(\mathbf{r})$  without any further changes.

For the piezoelectric potential, Eq. 16 for the spatially varying inverse dielectric constant assumed sharp interfaces. In the case of a smooth indium profile, we use Eq. 43 to write

$$\varepsilon(\mathbf{r}) = \varepsilon^{\text{B}} X(\mathbf{r}) + [1 - X(\mathbf{r})] \varepsilon^{\text{A}} \quad (48)$$

In the scenario where  $X(\mathbf{r})$  is spatially varying, Eq. 16 can no longer be applied, because the inverse of the dielectric constant is not a linear function of indium. However, similar to the band gap, we find that

$$\frac{1}{\varepsilon(\mathbf{r})} \approx \frac{1}{\varepsilon^{\text{d}}(X_0)} \chi_{\text{sm}}(\mathbf{r}) + [1 - \chi_{\text{sm}}(\mathbf{r})] \frac{1}{\varepsilon^{\text{A}}} \quad (49)$$

still gives an accurate representation of  $\varepsilon^{-1}(\mathbf{r})$ . Figure 10 shows a disagreement of less than 1 percent between the inverse dielectric from Eq. 48 and the linear interpolation in Eq. 49. The form of Eq. 49 allows us to use Eqs. 17-19 for the piezoelectric potential with a simple substitution of  $\chi(\mathbf{r})$  by  $\chi_{\text{sm}}(\mathbf{r})$ .

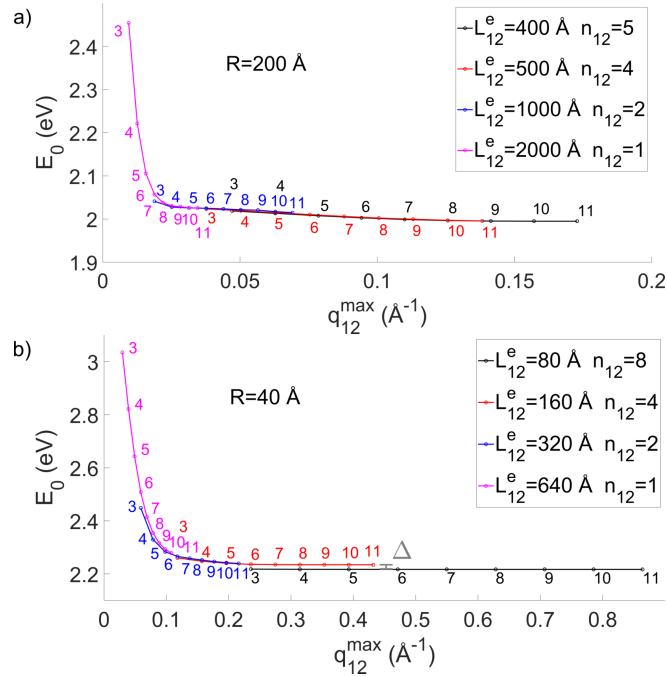


FIG. 11. Convergence of the fundamental gap of the quantum dot  $E_0$  for a 1D array of quantum dots with the maximum magnitude of  $q_{12}$  included in the  $\mathbf{k} \cdot \mathbf{p}$  calculations.  $L_{12}^e$  and  $n_{12}$  vary while (a) has  $R = 200\text{\AA}$  with strain box size held constant at  $L_{12}^s = 10R$  and (b) has  $R = 40\text{\AA}$  with  $L_{12}^s = 16R$ . Plane wave sampling  $m_{12}$  from 3 to 11 are shown for each choice of  $L_{12}^e$ ; the number next to each point indicates  $m_{12}$ . Different values of  $m_{12}$ ,  $L_{12}^e$  that produce the same  $q_{12}^{\text{max}}$  can be seen to produce approximately the same  $E_0$ , showing that  $q_{12}^{\text{max}}$  is a useful metric for convergence of these states. Since  $q_{12}^{\text{max}} = m_{12}\pi/L_{12}^e$  and computational cost scales with  $m_{12}$ , smaller  $L_{12}^e$  allows easier access to large  $q_{12}^{\text{max}}$ . In both panels, the black curves have  $L_{12}^e = 2R$ , so the dots touch each other at the 6 edges of the hexagonal unit cell. For larger dot, there is no visible deviation of  $E_0$  from the trend with separated dots. With the smaller dot, tunneling of the wavefunctions into neighboring dots causes  $E_0$  to have a significant change, labeled  $\Delta$ .

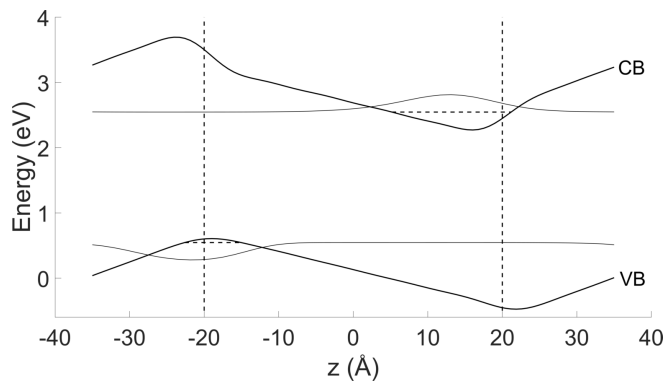


FIG. 12. Electronic structure of the QD superlattice system along the central axis of the dot for  $\delta = [1.5, 1.5, 2.5]\text{\AA}$ , corresponding to  $s = 1$  in Fig. 13(a). Other system parameters are in Table I. Lowest bound electron and hole states energies are shown by the horizontal dashed lines. Thick solid lines are the bulk band edges under the influence of the piezoelectric field and strain. Thin solid lines are  $z$ -axis projections of the probability distributions obtained from the envelope functions. Dashed vertical lines are the nominal material interfaces before smoothing. These calculations include spatially varying elastic and dielectric constants.

TABLE II. Energy shifts due to spatially varying  $\lambda(\mathbf{r})$  and  $\varepsilon(\mathbf{r})$  relative to the case with uniform constants of the host material  $\lambda^{\text{GaN}}$  and  $\varepsilon^{\text{GaN}}$ , respectively. System parameters in Table I.

Energy shifts	$\lambda(\mathbf{r})$ & $\varepsilon^{\text{GaN}}$	$\lambda^{\text{GaN}}$ & $\varepsilon(\mathbf{r})$	$\lambda(\mathbf{r})$ & $\varepsilon(\mathbf{r})$
$\Delta E_c$ (meV)	16.7	46.7	64.7
$\Delta E_v$ (meV)	-5.1	-30.6	-37.4
$\Delta E_0$ (meV)	21.7	77.4	102.1

## V. IMPACTS OF CORRECTIONS

In this section, we apply our methodology to study the case of a 1D array of quantum dots, such as described in Ref. [1], though we do not consider the boundaries of the nanowire. We achieve this 1D array by taking  $n_3 = 1$  to fully couple the dots in the  $z$ -direction and  $n_{12} > 1$  to avoid strain effects from neighboring dots in the  $xy$ -plane. In this section, we investigate convergence of the lowest electron and hole state energies  $E_c$  and  $E_v$ , which define the fundamental gap of the dot  $E_0 = E_c - E_v$ . More specifically, we show that the largest wave vector sampled plays a dominant role in convergence. We also show the energy shifts experienced by these two states when using uniform or spatially varying material parameters and when including alloy smoothing.

We model an infinite 1D quantum dot array with parameters listed in Table I. The 1D dot array has an experimentally well characterized dot-dot spacing in  $z$ , which fixes  $L_3^e = L_3^s = L_3$ , leaving  $L_{12}$  and  $n_{12}$  to be fixed. These quantum dots have a rather large radius, so the smallest spatial feature that we need to resolve is the decay of the bound wavefunctions into the classically forbidden region. Given that bound wavefunctions decay faster than strain, we need wave vectors that are relatively large to be able to resolve the wavefunctions. Increasing  $m_{12}$  increases the maximum wave vector contained in the mesh, but we can also sample at larger wave vectors by using a smaller  $L_{12}^e$ . However, if the electronic cell is chosen too small, then there can be electronic wavefunction overlap between states of neighboring dots. We must then choose  $L_{12}^e$  as small as possible while also avoiding dot-dot interactions. As for strain, in order to study a 1D array, we must choose  $n_{12}$  sufficiently large to have  $L_{12}^s = n_{12}L_{12}^e$  large enough that the strain of the quantum dot superlattice does not extend across neighboring strain unit cells in the  $xy$ -plane.

With this intuition, we turn to the convergence of  $E_0$  in terms of  $m_{12}$ ,  $L_{12}^e$  and  $n_{12}$ . Figure 11(a) shows the importance of the largest  $\mathbf{q}$  in the electronic mesh,  $q_{12}^{\text{max}}$ , for convergence of  $E_0$ . In this study,  $L_{12}^e$  and  $n_{12}$  are chosen to keep a constant  $L_{12}^s = L_{12}^e n_{12} = 2000\text{\AA}$ . We observe that  $E_0$  is to good approximation a function of only  $q_{12}^{\text{max}}$  and not of  $m_{12}$  and  $L_{12}^e$ , converging towards the same value for all choices of  $L_{12}^e$ . We also observe that the smallest  $L_{12}^e$  with highest  $m_{12}$  gives the most converged  $E_0$ , since  $q_{12}^{\text{max}} = m_{12}\pi/L_{12}^e$ . The black line in Fig. 11(a) represents the case of dots touching in the  $xy$  plane and, interestingly, does not break the convergence trend. However, we do find a break in the convergence trend for smaller dots in Fig. 11(b). This difference in convergence is due to the larger quantum dots having better confined states compared to the smaller dots. Smaller dots have wavefunctions that extend further outside the dot region, which makes them more able to tunnel to a neighboring dot. Consequently,

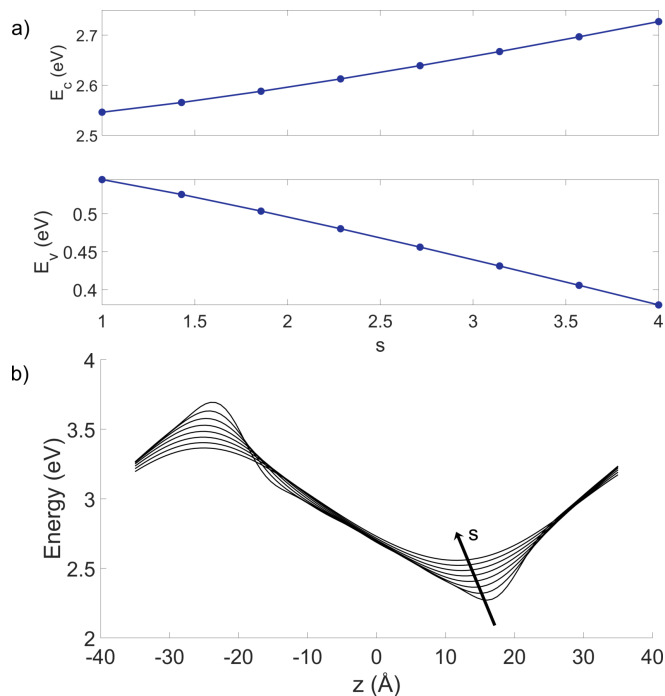


FIG. 13. Effects of indium diffusion, given by  $\delta = s[1.5, 1.5, 2.5]\text{\AA}$ , for (a)  $E_c$  and  $E_v$  and (b) bulk conduction band edge. Remaining parameters are as listed in Table I. Increase in indium diffusion leads to less confinement, which pushes the two states apart in energy, widening the electronic gap  $E_0$ . Electronic structure for  $s = 1$  is shown in Fig. 12.

care has to be taken in choosing the unit cell dimensions for small quantum dots.

The lowest quantum dot confined electron and hole energies,  $E_c$  and  $E_v$ , have respectively been converged within 5 meV by choosing  $m_{12}$ ,  $m_3$  and  $n_{12}$  sufficiently large, see Table I. Material parameters are listed in Appendix A. Band edges and lowest-energy confined states are shown in Fig. 12. The thick black solid lines represent the bulk band edges modified by the piezoelectric potential and strain. To include strain effects in the bulk band edges, we have used the (1, 1) matrix element from Eq. 26 to modify the conduction band edge and a third of the trace of the  $3 \times 3$  valence band block for the valence band edge.

The modifications in both the strain and piezoelectric potential due to spatially varying elastic and dielectric constants also have effects on the electronic structure. Table II shows how much  $E_v$  and  $E_c$  shift due to the corrections. We find that both corrections push the states apart, leading to an energy gap 100 meV larger than from simpler calculations with uniform  $\varepsilon$  and  $\lambda$ , a significant change that shows the importance of accurate modeling of dielectric and elastic parameters.

Figure 13(a) shows that indium diffusion pushes the lowest electron and hole states apart, which is due to changes in the confining potentials. From Fig. 13(b), we see that indium diffusion reduces the depth of the confining potential. We have observed similar behavior for the hole state confining potential, leading to  $E_v$  being pushed down in energy. Consequently, the gap  $E_0$  increases in energy as indium diffusion is increased.

In the case of sharp material interfaces, large wave vectors are needed to resolve the discontinuous parameter profiles. Smoothing removes the sharp interfaces and yields smoothly varying material parameters. Consequently, the required  $q_{12}^{\max}$  for the same degree of convergence is smaller, which means that smaller  $m_{12}$  and  $m_3$  and therefore reduced computational cost are needed with increasing  $\delta$ . In Figs. 13 (a) and (b), we converged for the case of  $s = 1$ , guaranteeing convergence for the rest of the sweep.

## VI. CONCLUSIONS

We have demonstrated techniques for and results of four modifications of standard quantum dot  $\mathbf{k} \cdot \mathbf{p}$  theory. We have included spatially varying elastic and dielectric constants as alloy fraction changes in strain and piezoelectric potential calculations. The effects of the spatially varying parameters are non-negligible on the strain and piezoelectric potential and also produce important shifts of the lowest electron and hole states, significantly changing the calculated gap of the quantum dot. We have also presented a method to include smoothly varying alloy profiles in Fourier-based

strain, piezoelectric potential and  $\mathbf{k} \cdot \mathbf{p}$  calculations. This smoothing has to be chosen to represent the device of interest, such as for indium diffusion in InGaN systems. For the case of  $\mathbf{k} \cdot \mathbf{p}$  theory for isolated dots, we have presented a new methodology of overlapping electronic and strain meshes to facilitate the coupling of strain into the  $\mathbf{k} \cdot \mathbf{p}$  Hamiltonian, greatly reducing the computational cost of calculating the Hamiltonian matrix elements. Lastly, we have shown that the maximum wave vector contained in the electronic sampling mesh is the most important criterion for determining convergence of quantum dot levels.

## ACKNOWLEDGMENTS

We acknowledge useful conversation with Stanko Tomić about Fourier-space  $\mathbf{k} \cdot \mathbf{p}$  methods. We acknowledge funding from the Ontario Early Researcher Award and NSERC CREATE TOP-SET program, Award number 497981.

## Appendix A: Bulk $\mathbf{k} \cdot \mathbf{p}$ parameters

From Ref. [7], the  $\mathbf{k} \cdot \mathbf{p}$  parameters  $A'_i$  are related to the Kane parameters  $P_i$  as

$$A'_1 = \frac{\hbar^2}{2m_e^{\parallel}} - \frac{P_1^2}{E_g}$$

$$A'_2 = \frac{\hbar^2}{2m_e^{\perp}} - \frac{P_2^2}{E_g}$$

where

$$P_1^2 = \frac{\hbar^2}{2m_0} \left( \frac{m_0}{m_e^{\parallel}} - 1 \right) \frac{3E_g (\Delta_{\text{so}} + E_g) + \Delta_{\text{cr}} (2\Delta_{\text{so}} + 3E_g)}{2\Delta_{\text{so}} + 3E_g}$$

$$P_2^2 = \frac{\hbar^2}{2m_0} \left( \frac{m_0}{m_e^{\perp}} - 1 \right) \frac{E_g [3E_g (\Delta_{\text{so}} + E_g)] + \Delta_{\text{cr}} (2\Delta_{\text{so}} + 3E_g)}{\Delta_{\text{cr}}\Delta_{\text{so}} + 3\Delta_{\text{cr}}E_g + 2\Delta_{\text{so}}E_g + E_g^2}.$$

Here,  $m_e^{\parallel}$  and  $m_e^{\perp}$  are the electron effective masses along the z-axis and in the xy-plane, respectively.  $\Delta_{\text{cr}}$  and  $\Delta_{\text{so}}$  are the crystal field splitting and spin-orbit coupling, respectively. The Luttinger-like parameters  $L'_i$ ,  $M_i$  and  $N'_i$  are related to the  $A_i$  parameters by

$$L'_1 = \frac{\hbar^2}{2m_0} (A_2 + A_4 + A_5) + \frac{P_2^2}{E_g}$$

$$L'_2 = \frac{\hbar^2}{2m_0} A_1 + \frac{P_1^2}{E_g}$$

$$M_1 = \frac{\hbar^2}{2m_0} (A_2 + A_4 - A_5)$$

$$M_2 = \frac{\hbar^2}{2m_0} (A_1 + A_3)$$

$$M_3 = \frac{\hbar^2}{2m_0} A_2$$

$$N'_1 = \frac{\hbar^2}{2m_0} 2A_5 + \frac{P_2^2}{E_g}$$

$$N'_2 = \frac{\hbar^2}{2m_0} \sqrt{2}A_6 + \frac{P_1 P_2}{E_g}$$

Note there is an error in the relations for  $L'_1$ ,  $L'_2$  and  $N'_1$  in Ref. [7], which we have corrected in agreement with Appendix B of Ref. [25]. The parameters  $A_i$ ,  $P_i$  and  $E_g$  used in our numerical study of InGaN systems are given in Table III.

Similarly to the  $\mathbf{k} \cdot \mathbf{p}$  parameters  $L'_i$ ,  $M_i$  and  $N'_i$ , the strain parameters are

$$\begin{aligned}
 l_1 &= D_2 + D_4 + D_5 \\
 l_2 &= D_1 \\
 m_1 &= D_2 + D_4 - D_5 \\
 m_2 &= D_1 + D_3 \\
 m_2 &= D_1 + D_3 \\
 m_3 &= D_2 \\
 n_1 &= 2D_5 \\
 n_2 &= \sqrt{2}D_6
 \end{aligned}$$

where the deformation potentials  $D_i$  are listed in Table III.

TABLE III. Material parameters used to model the InGaN system. Parameters were taken from Ref. [7].

Parameters	GaN	InN
$a$ (Å)	3.189	3.545
$c$ (Å)	5.185	5.703
$C_{11}$ (GPa)	390	223
$C_{12}$ (GPa)	145	115
$C_{13}$ (GPa)	106	92
$C_{33}$ (GPa)	398	224
$C_{44}$ (GPa)	105	48
$e_{15}$ (C/m <sup>2</sup> )	0.326	0.264
$e_{31}$ (C/m <sup>2</sup> )	-0.527	-0.484
$e_{33}$ (C/m <sup>2</sup> )	0.895	1.06
$P_{\text{sp}}$ (C/m <sup>2</sup> )	-0.034	-0.042
$\varepsilon_r$	9.8	13.8
$E_g$ (eV)	3.51	0.78
$E_v$ (eV)	0	0.5
$\Delta_{\text{cr}}$ (eV)	0.010	0.040
$\Delta_{\text{so}}$ (eV)	0.017	0.005
$m_{\parallel}/m_0$	0.20	0.07
$m_{\perp}/m_0$	0.20	0.07
$A_1$	-7.21	-8.21
$A_2$	-0.44	-0.68
$A_3$	6.68	7.57
$A_4$	-3.46	-5.23
$A_5$	-3.40	-5.11
$A_6$	-4.90	-5.96
$a_1$ (eV)	-4.9	-3.5
$a_2$ (eV)	-11.3	-3.5
$D_1$ (eV)	-3.7	-3.7
$D_2$ (eV)	4.5	4.5
$D_3$ (eV)	8.2	8.2
$D_4$ (eV)	-4.1	-4.1
$D_5$ (eV)	-4.0	-4.0
$D_6$ (eV)	-5.5	-5.5

### Appendix B: Characteristic functions

The characteristic function of a single dot is unity inside the dot and zero outside,

$$\chi_d(\mathbf{r}) = \begin{cases} 1 & \mathbf{r} \in \Omega_d \\ 0 & \text{otherwise} \end{cases}$$

where  $\Omega_d$  is the space inside the dot. For a cylindrical dot centered on the origin with radius  $R$  and height  $h$  along the  $z$ -axis, the Fourier transform of  $\chi_d$  is

$$\tilde{\chi}_d(\mathbf{q}) = \frac{1}{(2\pi)^3} \frac{4\pi R}{q_3 \sqrt{q_x^2 + q_y^2}} \sin\left(\frac{h}{2} q_3\right) J_1\left(R \sqrt{q_x^2 + q_y^2}\right).$$

The characteristic function of the electronic cell, the hexagonal prism shown in Fig. 1, is defined as

$$\chi_e(\mathbf{r}) = \begin{cases} 1 & \mathbf{r} \in \Omega_e \\ 0 & \text{otherwise} \end{cases}$$

and its Fourier transform is

$$\tilde{\chi}_e(\mathbf{q}) = L_3 \text{sinc}\left(q_3 \frac{L_3}{2}\right) \frac{q_1 \cos\left(\frac{L_{12} q_1}{2}\right) + q_2 \cos\left(\frac{L_{12} q_2}{2}\right) - (q_1 + q_2) \cos\left(L_{12} \frac{q_1 + q_2}{2}\right)}{\sqrt{3} q_1 q_2 (q_1 + q_2)}.$$

### Appendix C: Fourier and Convolution Conventions

We define the Fourier forward and inverse transforms of a function  $g(\mathbf{r})$  as

$$\mathcal{F}\{g(\mathbf{r})\}(\mathbf{q}) \equiv \tilde{g}(\mathbf{q}) = \frac{1}{(2\pi)^3} \int_{-\infty}^{\infty} d^3\mathbf{r} g(\mathbf{r}) e^{-i\mathbf{q}\cdot\mathbf{r}}$$

$$\mathcal{F}^{-1}\{\tilde{g}(\mathbf{q})\}(\mathbf{r}) = g(\mathbf{r}) = \int_{-\infty}^{\infty} d^3\mathbf{q} \tilde{g}(\mathbf{q}) e^{i\mathbf{q}\cdot\mathbf{r}}$$

A convolution is denoted by

$$(f * g)(\mathbf{r}) = \int_{-\infty}^{\infty} f(\mathbf{r}') g(\mathbf{r} - \mathbf{r}') d\mathbf{r}'$$

The convolution theorem states

$$(\tilde{f} * \tilde{g})(\mathbf{q}) = \mathcal{F}\{f(\mathbf{r}) g(\mathbf{r})\}(\mathbf{q}).$$

For a system that is periodic in real space with a unit cell  $\Omega$  of volume  $V$ , we define

$$\tilde{g}(\mathbf{q}) = \frac{1}{V} \int_{\Omega} d^3\mathbf{r} g(\mathbf{r}) e^{-i\mathbf{q}\cdot\mathbf{r}}$$

$$g(\mathbf{r}) = \sum_{\mathbf{q} \in \Omega^{-1}} \tilde{g}(\mathbf{q}) e^{i\mathbf{q}\cdot\mathbf{r}}$$

where  $\Omega^{-1}$  is the reciprocal space to the unit cell  $\Omega$ . Defining the Fourier space convolution as

$$(\tilde{f} * \tilde{g})(\mathbf{q}) = \sum_{\mathbf{q}' \in \Omega^{-1}} \tilde{f}(\mathbf{q}') \tilde{g}(\mathbf{q} - \mathbf{q}'), \quad (\text{C1})$$

the convolution theorem is

$$\left(\tilde{f} * \tilde{g}\right)(\mathbf{q}) = \mathcal{F}\{f(\mathbf{r})g(\mathbf{r})\}(\mathbf{q}).$$

Since we consider different superlattice unit cells for the electronic and strain properties,  $\left(\tilde{f} * \tilde{g}\right)_e$  indicates a convolution on the electronic space  $\Omega_e^{-1}$  and  $\left(\tilde{f} * \tilde{g}\right)_s$  on the strain space  $\Omega_s^{-1}$ .

The reciprocal space  $\Omega^{-1}$  contains a discrete infinity of wave vectors on which to evaluate  $\tilde{f}$  and  $\tilde{g}$ . The convolution in Eq. C1 then sums over the infinite number of wave vectors, with  $\tilde{f}$  and  $\tilde{g}$  being functions that decay at large wave vectors. For the calculations in this manuscript, we choose a finite number of wave vectors. By choosing this mesh to contain wave vectors sufficiently large to capture the decay of  $\tilde{f}$  and  $\tilde{g}$ , we can calculate the linear convolution in Eq. C1 to good approximation by padding the  $\tilde{f}$  and  $\tilde{g}$  arrays with zeros and performing a circular convolution, defined below.

We denote the finite Fourier-space mesh by  $\mathbf{q}_{i_1 i_2 i_3}$  with  $-m_j < i_j < m_j$  such that  $N_j = 2m_j + 1$  is the dimension of the mesh in each direction. For simplicity, we use the mapping  $p_j = i_j + m_j + 1$  to start indexing from 1. Evaluating a function  $\tilde{f}$  on the mesh  $\mathbf{q}_{p_1 p_2 p_3}$  gives the array  $\tilde{f}_{p_1 p_2 p_3}$ . The Fourier-space array  $\tilde{f}_{p_1 p_2 p_3}$  and its real-space counterpart  $f_{v_1 v_2 v_3}$  are then related through the discrete Fourier transform and its inverse,

$$\tilde{f}_{p_1 p_2 p_3} = \mathcal{F}\{f\}_{p_1 p_2 p_3} = \frac{1}{N} \sum_{v_1, v_2, v_3=1}^{N_1, N_2, N_3} f_{v_1 v_2 v_3} e^{-i2\pi(p_1 v_1 / N_1 + p_2 v_2 / N_2 + p_3 v_3 / N_3)} \quad (\text{C2})$$

$$f_{v_1 v_2 v_3} = \mathcal{F}^{-1}\{\tilde{f}\}_{v_1 v_2 v_3} = \sum_{p_1, p_2, p_3=1}^{N_1, N_2, N_3} \tilde{f}_{p_1 p_2 p_3} e^{i2\pi(p_1 v_1 / N_1 + p_2 v_2 / N_2 + p_3 v_3 / N_3)}. \quad (\text{C3})$$

where  $N = N_1 N_2 N_3$ . The circular convolution is defined as

$$\left(\tilde{f} \bullet \tilde{g}\right)_{p_1 p_2 p_3} = \sum_{p'_1, p'_2, p'_3=1}^{N_1, N_2, N_3} \tilde{f}_{p'_1 p'_2 p'_3} \tilde{g}_{(p_1 - p'_1), (p_2 - p'_2), (p_3 - p'_3)}$$

where  $\tilde{f}_{(p_1 + N_1), (p_2 + N_2), (p_3 + N_3)} = \tilde{f}_{p_1 p_2 p_3}$  and likewise for  $\tilde{g}$ . The convolution theorem is then

$$\left(\tilde{f} \bullet \tilde{g}\right)_{p_1 p_2 p_3} = \mathcal{F}\{fg\}_{p_1 p_2 p_3}.$$

To perform a linear convolution, we pad the arrays with zeros, which increases the dimensions of the mesh to  $N_j^p = N_j + 2m_j$  and yields the padded array  $\tilde{f}_{p_1 p_2 p_3}^p$  containing  $N^p = N_1^p N_2^p N_3^p$  elements. The linear convolution is then

$$\left(\tilde{f} * \tilde{g}\right)_{p_1 p_2 p_3} = \left(\tilde{f}^p \bullet \tilde{g}^p\right)_{p_1 p_2 p_3} \quad (\text{C4})$$

This result is independent of the basis used to generate the mesh and is valid in the case of hexagonal meshes.

#### Appendix D: Displacement field Green's tensor

The Green's function for the displacement field for spatially varying elastic constants must satisfy [8]

$$\frac{\partial}{\partial x_k} \lambda_{iklm}(\mathbf{r}) \frac{\partial}{\partial x_m} G_{ln}(\mathbf{r} - \mathbf{r}') = -\delta(\mathbf{r} - \mathbf{r}') \delta_{in}$$

From Ref. [8], the Green's tensor when  $\lambda_{jklm}$  is spatially invariant is

$$\tilde{G}_{in}^h = \frac{1}{(2\pi)^3} \frac{1}{\beta q^2 + \rho q_3^2} \left\{ \delta_{in} - [(\rho q^2 + \gamma q_3^2) \delta_{i3} + (\kappa + \rho) q_i q_3] \frac{F \delta_{3n} - I}{FP - IQ} q_n - [(\alpha + \beta) q_i + (\kappa + \rho) \delta_{i3} q_3] \frac{P - Q \delta_{3n}}{FP - IQ} q_n \right\},$$

where

$$\begin{aligned}
F(\mathbf{q}) &= (C_{13} + 2C_{44} - C_{11})q_3^2 + C_{11}q^2 \\
Q(\mathbf{q}) &= (C_{33} - 2C_{13} - 4C_{44} + C_{11})q_3^2 + (C_{13} + 2C_{44} - C_{11})q^2 \\
P(\mathbf{q}) &= C_{44}q^2 + (C_{33} - C_{13} - 2C_{44})q_3^2 \\
I(\mathbf{q}) &= (C_{13} + C_{44})q_3^2 \\
\alpha &= C_{12} \\
\beta &= \frac{1}{2}(C_{11} - C_{12}) \\
\gamma &= C_{33} - 2C_{13} - 4C_{44} + C_{11} \\
\kappa &= C_{13} - C_{12} \\
\rho &= C_{44} + \frac{C_{12} - C_{11}}{2}
\end{aligned}$$

with  $C_{ij}$  being the elastic constants.

### Appendix E: Polarization fields

There are two contributions to the piezoelectric polarization fields: strain driven and spontaneous. The strain-driven polarization can be written [10]

$$\begin{bmatrix} P_1^{\text{st}} \\ P_2^{\text{st}} \\ P_3^{\text{st}} \end{bmatrix} = \begin{bmatrix} 2e_{15}\epsilon_{13} \\ 2e_{15}\epsilon_{23} \\ e_{31}(\epsilon_{11} + \epsilon_{22}) + e_{33}\epsilon_{33} \end{bmatrix},$$

where  $e_{ij}$  are the piezoelectric constants and  $\epsilon_{ij}$  the strain fields. We write the piezoelectric constants using the characteristic function of the quantum dot

$$e_{ij}(\mathbf{r}) = e_{ij}^{\text{d}}\chi_{\text{d}}(\mathbf{r}) + e_{ij}^{\text{h}}[1 - \chi_{\text{d}}(\mathbf{r})].$$

The Fourier transform of the polarization fields is then

$$\begin{bmatrix} \tilde{P}_1^{\text{st}} \\ \tilde{P}_2^{\text{st}} \\ \tilde{P}_3^{\text{st}} \end{bmatrix} = \begin{bmatrix} 2e_{15}^{\text{h}}\tilde{\epsilon}_{13}(\mathbf{q}) + \frac{2(2\pi)^3(e_{15}^{\text{d}} - e_{15}^{\text{h}})}{V}(\tilde{\chi}_{\text{d}} * \tilde{\epsilon}_{13})_e(\mathbf{q}) \\ 2e_{15}^{\text{h}}\tilde{\epsilon}_{23}(\mathbf{q}) + \frac{2(2\pi)^3(e_{15}^{\text{d}} - e_{15}^{\text{h}})}{V}(\tilde{\chi}_{\text{d}} * \tilde{\epsilon}_{23})_e(\mathbf{q}) \\ e_{31}^{\text{h}}[\tilde{\epsilon}_{11}(\mathbf{q}) + \tilde{\epsilon}_{22}(\mathbf{q})] + \frac{(2\pi)^3(e_{31}^{\text{d}} - e_{31}^{\text{h}})}{V}[\tilde{\chi}_{\text{d}} * (\tilde{\epsilon}_{11} + \tilde{\epsilon}_{22})]_e(\mathbf{q}) + e_{33}^{\text{h}}\tilde{\epsilon}_{33}(\mathbf{q}) + \frac{(2\pi)^3(e_{33}^{\text{d}} - e_{33}^{\text{h}})}{V}(\tilde{\chi}_{\text{d}} * \tilde{\epsilon}_{33})_e(\mathbf{q}) \end{bmatrix}$$

In a bulk wurtzite material, the spontaneous polarization is along the  $c$ -axis and uniform throughout the material

$$\mathbf{P}^{\text{sp}}(\mathbf{r}) = \begin{bmatrix} 0 \\ 0 \\ P^{\text{sp}} \end{bmatrix}$$

Then

$$\tilde{P}_3^{\text{sp}}(\mathbf{q}) = P^{\text{sp,h}}\delta_{\mathbf{q},0} + (P^{\text{sp,d}} - P^{\text{sp,h}})\tilde{\chi}(\mathbf{q})$$

where  $P^{\text{sp,d}}$  and  $P^{\text{sp,h}}$  are the spontaneous polarizations in the dot and host materials, respectively.

### Appendix F: QD $\mathbf{k} \cdot \mathbf{p}$ Hamiltonian

For the quantum dot superlattice system, the  $\mathbf{k} \cdot \mathbf{p}$  Hamiltonian matrix elements of Eq. 37 in the symmetry adapted basis are given in terms of the parameters  $f_{\alpha'\alpha}^{\text{d}}$  and  $f_{\alpha'\alpha}^{\text{h}}$  that make up the bulk  $\mathbf{k} \cdot \mathbf{p}$  Hamiltonian matrix elements  $H_{\alpha'\alpha}$ , presented in Sec. III. We take the convention where superscript “(0)” indicates a bulk Hamiltonian matrix



element containing no wave vector, “(i)” indicates a single wave vector  $k_i$  and “(i, j)” two wave vectors  $k_i$  and  $k_j$ . By defining  $\phi = \frac{2\pi}{6}$  and

$$S_{\alpha',\alpha}^{ll'm_f} = e^{i\phi\{l[m_f - J_z(\alpha)] - l'[m_f - J_z(\alpha')]\}}$$

$$S_{\alpha'}^{l'm_f} = e^{-il'\phi[m_f - J_z(\alpha')]},$$

the quantum dot Hamiltonian matrix elements are

$$\mathcal{H}_{m_f\alpha'\alpha}^{(0)}(\mathbf{q}', \mathbf{q}) = \frac{1}{6} \sum_{l'=0}^5 \sum_{l=0}^5 S_{\alpha',\alpha}^{ll'm_f} h_{\alpha'\alpha}(\vec{\mathbf{R}}_{l'}\mathbf{q}', \vec{\mathbf{R}}_l\mathbf{q})$$

$$\mathcal{H}_{m_f\alpha'\alpha}^{(i)}(\mathbf{q}', \mathbf{q}) = \frac{1}{6} \sum_{l'=0}^5 \sum_{l=0}^5 S_{\alpha',\alpha}^{ll'm_f} \frac{(\vec{\mathbf{R}}_{l'}\mathbf{q}')_i + (\vec{\mathbf{R}}_l\mathbf{q})_i}{2} h_{\alpha'\alpha}(\vec{\mathbf{R}}_{l'}\mathbf{q}', \vec{\mathbf{R}}_l\mathbf{q})$$

$$\mathcal{H}_{m_f\alpha'\alpha}^{(i,j)}(\mathbf{q}', \mathbf{q}) = \frac{1}{6} \sum_{l'=0}^5 \sum_{l=0}^5 S_{\alpha',\alpha}^{ll'm_f} \frac{(\vec{\mathbf{R}}_l\mathbf{q})_j (\vec{\mathbf{R}}_{l'}\mathbf{q}')_i + (\vec{\mathbf{R}}_l\mathbf{q})_i (\vec{\mathbf{R}}_{l'}\mathbf{q}')_j}{2} h_{\alpha'\alpha}(\vec{\mathbf{R}}_{l'}\mathbf{q}', \vec{\mathbf{R}}_l\mathbf{q})$$

$$\mathcal{H}_{m_f\alpha'\alpha}^{(0)}(\mathbf{q}', \mathbf{q}_z) = \frac{1}{\sqrt{6}} \sum_{l'=0}^5 S_{\alpha'}^{l'm_f} h_{\alpha'\alpha}(\vec{\mathbf{R}}_{l'}\mathbf{q}', \mathbf{q}_z)$$

$$\mathcal{H}_{m_f\alpha'\alpha}^{(i)}(\mathbf{q}', \mathbf{q}_z) = \frac{1}{\sqrt{6}} \sum_{l'=0}^5 S_{\alpha'}^{l'm_f} \frac{(\vec{\mathbf{R}}_{l'}\mathbf{q}')_i + (\mathbf{q}_z)_i}{2} h_{\alpha'\alpha}(\vec{\mathbf{R}}_{l'}\mathbf{q}', \mathbf{q}_z)$$

$$\mathcal{H}_{m_f\alpha'\alpha}^{(i,j)}(\mathbf{q}', \mathbf{q}_z) = \frac{1}{\sqrt{6}} \sum_{l'=0}^5 S_{\alpha'}^{l'm_f} \frac{(\mathbf{q}_z)_j (\vec{\mathbf{R}}_{l'}\mathbf{q}')_i + (\mathbf{q}_z)_i (\vec{\mathbf{R}}_{l'}\mathbf{q}')_j}{2} h_{\alpha'\alpha}(\vec{\mathbf{R}}_{l'}\mathbf{q}', \mathbf{q}_z)$$

$$\mathcal{H}_{m_f\alpha'\alpha}^{(0)}(\mathbf{q}'_z, \mathbf{q}_z) = h_{\alpha'\alpha}(\mathbf{q}'_z, \mathbf{q}_z)$$

$$\mathcal{H}_{m_f\alpha'\alpha}^{(i)}(\mathbf{q}'_z, \mathbf{q}_z) = \frac{(\mathbf{q}'_z)_i + (\mathbf{q}_z)_i}{2} h_{\alpha'\alpha}(\mathbf{q}'_z, \mathbf{q}_z)$$

$$\mathcal{H}_{m_f\alpha'\alpha}^{(i,j)}(\mathbf{q}'_z, \mathbf{q}_z) = \frac{(\mathbf{q}_z)_j (\mathbf{q}'_z)_i + (\mathbf{q}_z)_i (0, 0, \mathbf{q}'_z)_j}{2} h_{\alpha'\alpha}(\mathbf{q}'_z, \mathbf{q}_z)$$

where

$$h_{\alpha'\alpha}(\vec{\mathbf{R}}_{l'}\mathbf{q}', \vec{\mathbf{R}}_l\mathbf{q}) = f_{\alpha'\alpha}^h \delta_{l,l'} \delta_{\mathbf{q},\mathbf{q}'} + \frac{(2\pi)^3 (f_{\alpha'\alpha}^d - f_{\alpha'\alpha}^h)}{V} \tilde{\chi}_d(\vec{\mathbf{R}}_{l'}\mathbf{q}' - \vec{\mathbf{R}}_l\mathbf{q})$$

The contributions of the piezoelectric potential to the Hamiltonian are

$$\mathcal{H}_{m_f\alpha'\alpha}^{\text{pz}}(\mathbf{q}', \mathbf{q}) = -\delta_{\alpha',\alpha} \frac{(2\pi)^3 e_c}{6V} \sum_{l'=0}^5 \sum_{l=0}^5 e^{i\phi(l-l')[m_f - J_z(\alpha)]} \tilde{\varphi}(\vec{\mathbf{R}}_{l'}\mathbf{q}' - \vec{\mathbf{R}}_l\mathbf{q})$$

$$\mathcal{H}_{m_f\alpha'\alpha}^{\text{pz}}(\mathbf{q}', \mathbf{q}_z) = -\delta_{\alpha',\alpha} \frac{(2\pi)^3 e_c}{V\sqrt{6}} \sum_{l'=0}^5 e^{-il'\phi[m_f - J_z(\alpha')]} \tilde{\varphi}(\vec{\mathbf{R}}_{l'}\mathbf{q}' - \mathbf{q}_z)$$

$$\mathcal{H}_{m_f\alpha'\alpha}^{\text{pz}}(\mathbf{q}'_z, \mathbf{q}_z) = -\delta_{\alpha',\alpha} \frac{(2\pi)^3 e_c}{V} \tilde{\varphi}(\mathbf{q}'_z - \mathbf{q}_z)$$

where  $\tilde{\varphi}$  is described in Secs. II C and III C and  $e_c$  is the electric charge.

- 
- [1] H. P. T. Nguyen, S. Zhang, K. Cui, X. Han, S. Fatholoulumi, M. Couillard, G. A. Botton, and Z. Mi, “p-Type Modulation Doped InGaN/GaN Dot-in-a-Wire White-Light-Emitting Diodes Monolithically Grown on Si(111),” *Nano Lett.* **11**, 1919–1924 (2011).
- [2] Tim J. Puchtler, Tong Wang, Christopher X. Ren, Fengzai Tang, Rachel A. Oliver, Robert A. Taylor, and Tongtong Zhu, “Ultrafast, Polarized, Single-Photon Emission from m-Plane InGaN Quantum Dots on GaN Nanowires,” *Nano Lett.* **16**, 7779–7785 (2016).
- [3] Md G. Kibria, Hieu P.T. Nguyen, Kai Cui, Songrui Zhao, Dongping Liu, Hong Guo, Michel L. Trudeau, Suzanne Paradis, Abou Rachid Hakima, and Zetian Mi, “One-step overall water splitting under visible light using multiband InGaN/GaN nanowire heterostructures,” *ACS Nano* **7**, 7886–7893 (2013).
- [4] Liwen Sang, Meiyong Liao, Qifeng Liang, Masaki Takeguchi, Benjamin Dierre, Bo Shen, Takashi Sekiguchi, Yasuo Koide, and Masatomo Sumiya, “A Multilevel Intermediate-Band Solar Cell by InGaN/GaN Quantum Dots with a Strain-Modulated Structure,” *Adv. Mater.* **26**, 1414–1420 (2014).
- [5] Ross Cheriton, Sharif M. Sadaf, Luc Robichaud, Jacob J. Krich, Zetian Mi, and Karin Hinzer, “Two-photon photocurrent in InGaN/GaN nanowire intermediate band solar cells,” *Communications Materials* **1**, 63 (2020).
- [6] T. Saito and Y. Arakawa, “Electronic structure of piezoelectric  $\text{In}_{0.2}\text{Ga}_{0.8}\text{N}$  quantum dots in GaN calculated using a tight-binding method,” *Physica E* **15**, 169–181 (2002).
- [7] Momme Winkelkemper, Andrei Schliwa, and Dieter Bimberg, “Interrelation of structural and electronic properties in  $\text{In}_x\text{Ga}_{1-x}\text{N}/\text{GaN}$  quantum dots using an eight-band k·p model,” *Phys. Rev. B* **74**, 155322 (2006).
- [8] A. D. Andreev and E. P. O’Reilly, “Theory of the electronic structure of GaN/AlN hexagonal quantum dots,” *Phys. Rev. B* **62**, 15851–15870 (2000).
- [9] Nenad Vukmirović, Dragan Indjin, Vladimir D. Jovanović, Zoran Ikonić, and Paul Harrison, “Symmetry of k·p Hamiltonian in pyramidal InAs/GaAs quantum dots: Application to the calculation of electronic structure,” *Phys. Rev. B* **72**, 075356 (2005).
- [10] Nenad Vukmirović, Zoran Ikonić, Dragan Indjin, and Paul Harrison, “Symmetry-based calculation of single-particle states and intraband absorption in hexagonal GaN/AlN quantum dot superlattices,” *J. Phys. Condens. Matter* **18**, 6249–6262 (2006).
- [11] Nenad Vukmirović and Stanko Tomić, “Plane wave methodology for single quantum dot electronic structure calculations,” *J. Appl. Phys.* **103**, 103718 (2008).
- [12] O. Stier, M. Grundmann, and D. Bimberg, “Electronic and optical properties of strained quantum dots modeled by 8-band k·p theory,” *Phys. Rev. B* **59**, 5688–5701 (1999).
- [13] A. D. Andreev, J. R. Downes, D. A. Faux, and E. P. O’Reilly, “Strain distributions in quantum dots of arbitrary shape,” *J. Appl. Phys.* **86**, 297–305 (1999).
- [14] J. Renard, R. Songmuang, G. Tourbot, C. Bougerol, B. Daudin, and B. Gayral, “Evidence for quantum-confined stark effect in gan/aln quantum dots in nanowires,” *Phys. Rev. B* **80**, 121305 (2009).
- [15] A. V. Nenashev, A. A. Koshkarev, and A. V. Dvurechenskii, “Approximate analytical description of the elastic strain field due to an inclusion in a continuous medium with cubic anisotropy,” *Journal of Applied Physics* **123**, 105104 (2018).
- [16] Fabio Bernardini, Vincenzo Fiorentini, and David Vanderbilt, “Spontaneous polarization and piezoelectric constants of III-V nitrides,” *Phys. Rev. B* **56**, R10024–R10027 (1997).
- [17] Agostino Zoroddu, Fabio Bernardini, Paolo Ruggerone, and Vincenzo Fiorentini, “First-principles prediction of structure, energetics, formation enthalpy, elastic constants, polarization, and piezoelectric constants of AlN, GaN, and InN: Comparison of local and gradient-corrected density-functional theory,” *Phys. Rev. B* **64**, 045208 (2001).
- [18] S. F. Chichibu, A. C. Abare, M. S. Minsky, S. Keller, S. B. Fleischer, J. E. Bowers, E. Hu, U. K. Mishra, L. A. Coldren, S. P. DenBaars, and T. Sota, “Effective band gap inhomogeneity and piezoelectric field in ingan/gan multiquantum well structures,” *Applied Physics Letters* **73**, 2006–2008 (1998).
- [19] J. P. Ibbetson, P. T. Fini, K. D. Ness, S. P. DenBaars, J. S. Speck, and U. K. Mishra, “Polarization effects, surface states, and the source of electrons in algan/gan heterostructure field effect transistors,” *Applied Physics Letters* **77**, 250–252 (2000).
- [20] Hwa-mok Kim, Yong-hoon Cho, Hosang Lee, Suk Il Kim, Sung Ryong Ryu, Deuk Young Kim, Tae Won Kang, and Kwan Soo Chung, “High-Brightness Light Emitting Diodes Using Dislocation-Free Indium Gallium Nitride/Gallium Nitride Multiquantum-Well Nanorod Arrays,” *Nano Letters* **4**, 1059–1062 (2004).
- [21] S. L. Chuang and C. S. Chang, “k·p method for strained wurtzite semiconductors,” *Phys. Rev. B* **54**, 2491–2504 (1996).
- [22] Milan Jocić Jocić and Nenad Vukmirović, “Ab initio construction of symmetry-adapted k·p hamiltonians for the electronic structure of semiconductors,” *Phys. Rev. B* **102**, 085121 (2020).
- [23] Stanko Tomić, Andrew G. Sunderland, and Ian J. Bush, “Parallel multi-band k·p code for electronic structure of zinc blend semiconductor quantum dots,” *J. Mater. Chem.* **16**, 1963–1972 (2006).
- [24] Richard A. Morrow and Kenneth R. Brownstein, “Model effective-mass Hamiltonians for abrupt heterojunctions and the associated wave-function-matching conditions,” *Phys. Rev. B* **30**, 678–680 (1984).
- [25] E. Berkowicz, D. Gershoni, G. Bahir, E. Lakin, D. Shilo, E. Zolotoyabko, A. C. Abare, S. P. Denbaars, and L. A. Coldren,

“Measured and calculated radiative lifetime and optical absorption of  $\text{In}_x\text{Ga}_{1-x}\text{N}/\text{GaN}$  quantum structures,” *Phys. Rev. B* **61**, 10994–11008 (2000).